RAA 2020 Vol. **20** No. **5**, 64(28pp) doi: 10.1088/1674–4527/20/5/64

http://www.raa-journal.org *http://iopscience.iop.org/raa*

***R**esearch in*
***A**stronomy and*
***A**strophysics*

The fundamental performance of FAST with 19-beam receiver at L band

Peng Jiang[1,2], Ning-Yu Tang[1,2], Li-Gang Hou[1,2], Meng-Ting Liu[1,2,3], Marko Krčo[1,2], Lei Qian[1,2], Jing-Hai Sun[1,2], Tao-Chung Ching[1,2], Bin Liu[1,2], Yan Duan[1,2,3], You-Ling Yue[1,2], Heng-Qian Gan[1,2], Rui Yao[1,2], Hui Li[1,2], Gao-Feng Pan[1,2], Dong-Jun Yu[1,2], Hong-Fei Liu[1,2], Di Li[1,2], Bo Peng[1,2], Jun Yan[1,2] and FAST Collaboration[1]

[1] National Astronomical Observatories, Chinese Academy of Sciences, Beijing 100101, China; *pjiang@nao.cas.cn, nytang@nao.cas.cn, ghq@nao.cas.cn*

[2] CAS Key Laboratory of FAST, National Astronomical Observatories, Chinese Academy of Sciences, Beijing 100101, China

[3] School of Astronomy and Space Science, University of Chinese Academy of Sciences, Beijing 100049, China

Received 2019 October 8; accepted 2020 February 2

Abstract The Five-hundred-meter Aperture Spherical radio Telescope (FAST) has passed national acceptance and finished one pilot cycle of 'Shared-Risk' observations. It will start formal operation soon. In this context, this paper describes testing results of key fundamental parameters for FAST, aiming to provide basic support for observation and data reduction of FAST for scientific researchers. The 19-beam receiver covering 1.05–1.45 GHz was utilized for most of these observations. The fluctuation in electronic gain of the system is better than 1% over 3.5 hours, enabling enough stability for observations. Pointing accuracy, aperture efficiency and system temperature are three key parameters for FAST. The measured standard deviation of pointing accuracy is $7.9''$, which satisfies the initial design of FAST. When zenith angle is less than $26.4°$, the aperture efficiency and system temperature around 1.4 GHz are $\sim$0.63 and less than 24 K for central beam, respectively. The sensitivity and stability of the 19-beam backend are confirmed to satisfy expectation by spectral HI observations toward NGC 672 and polarization observations toward 3C 286. The performance allows FAST to take sensitive observations for various scientific goals, from studies of pulsars to galaxy evolution.

Key words: instrumentation: detectors — line: profiles

1 INTRODUCTION

The Five-hundred-meter Aperture Spherical radio Telescope (FAST) with a diameter of 500 m passed its national acceptance on 2020 January 11. It operates at frequencies ranging from 70 to 3000 MHz and is the most sensitive single dish telescope in this frequency range.

FAST commissioning began when construction was completed on 2016 September 25. The details of FAST commissioning have been introduced in Jiang et al. (2019). A lot of observations, especially pulsar related observations, were taken during the commissioning phase. A series of primary results including the first detection of a pulsar by FAST have been published in the FAST special issue of Science China Physics, Mechanics & Astronomy (Qian et al. 2019; Lu et al. 2019a, b; Yu et al. 2019; Wang et al. 2019; Zhang et al. 2019).

Through efforts of the commissioning group, the performance of FAST has been improved significantly during the last two years. One example is the much improved radio frequency interference (RFI) environment. In this paper we will review the current instrumental properties based on measurements with the 19 beam receiver that covers 1.05 to 1.45 GHz.

In Section 2, we present the properties of the 19 beam receiver system including calibration of the noise dipole, the spatial distribution of all 19 beams, pointing accuracy, aperture efficiency and system temperature. In Section 3,

the performance of the spectral backend, including stability and sensitivity, standing waves and polarization, is presented. Observation modes and status of RFI are described in Section 4. A summary is provided in Section 5.

2 PROPERTIES OF THE 19 BEAM RECEIVER

2.1 Measurement of the Noise Dipole

The FAST 19-beam L-band Array contains a temperature stabilized noise injection system. The noise is injected between the feed and the low noise amplifiers. The noise source is a single diode whose signal is split into each beam and polarization. The diode itself is always powered, but it can be switched in and out of the signal path using a solid state switch. This was done in order to improve stability at very high switching speeds. It takes less than 1 microsecond for the noise power to stabilize once switched on or off. The noise diode has two adjustable power output modes, but these are currently kept at approximately 1.1 and 12.5 K.

In order to test the performance and stability of the noise diode, we conducted a series of hot load measurements whereby the feed cabin was lowered to the ground and a foam absorber was placed directly under the feed so that it completely covered all of the beams. We then periodically measured the temperature of the absorber with a thermometer, while the noise diode was continuously switched on and off ("a winking CAL") with a period of 1.00663296 s. Figure 1 and Figure 2 display the measured noise diode temperatures ($T_{\rm cal}$) for both the low and high power modes with respect to frequency. The diode is tuned so as to minimize the diode temperatures near 1420.4 MHz to reduce the impact on the system temperature.

Figure 3 depicts the fluctuations in electronic gain of the system over several hours. This was done assuming that the noise diode temperature is absolutely constant. It demonstrates that the electronic gain fluctuations within the FAST 19-beam receiver/backend signal path are typically on the order of a few percent over timescales of a few minutes. This implies that science projects for whom flux calibration is important should fire the noise diode at least every few minutes in order to account for typical electronic gain fluctuations. The larger fluctuations in Figure 3 are caused by RFI leaking into the signal path during the hot load measurements, and instability in the low noise amplifiers. The electronic gain fluctuations of the other beams are presented in Figure A.1.

Fluctuations in the electronic gain in Figure 3 are mostly uncorrelated between the different beams. By taking a median value of all 19 beams, we can produce Figure 4 which yields an upper limit on the temperature fluctuations in the noise diode. While laboratory measurements of the noise diode itself yielded temperature fluctuations on the order of $\sim 0.1\%$ over several hours, we see that once placed within the full signal path we get an upper limit of $\sim 1\%$, implying that it is likely impossible to obtain accurate flux calibration better than $\sim 1\%$. Considering FAST's pointing accuracy and beam size, the best flux calibration for a point source is approximately $\sim 2\%$, meaning that the noise diode is certainly operating within our tolerance limits. This lower limit is estimated by looking at the shape of the beam response function at 1420 MHz within the pointing uncertainty limits. The effect is weaker at longer wavelengths where the pointing uncertainty is smaller compared to the beam size.

2.2 Beam Properties and Pointing Accuracy

To measure the properties of FAST's 19-beam receiver, one method is to directly make mapping observations toward radio sources on the sky. The raster scan (or raster scanning) observation mode has been realized for FAST, which is used to map radio sources and measure the 19-beam properties.

2.2.1 Observations

From 2018 November 28 to December 29, mapping observations have been conducted toward 3C 380, 1902+319, 1859+129, 3C 454.3, 2023+318, etc. In the observations, a sky area centered on the target source and covering $\sim 37'({\rm RA}) \times 37'({\rm Dec})$ is mapped by a raster scan along the right ascension (RA) or declination (Dec) directions with the 19-beam receiver. An example of the telescope track for a raster scan along Dec is given in Figure 5. The scan velocity is $15'\,{\rm min}^{-1}$. The separation between two sub-scans is $1'$, which satisfies Nyquist sampling. A total of $\sim$100 minutes is needed to acquire such a map. Observational data are simultaneously recorded with the pulsar mode, the narrow-band spectral-line mode and also the wide-band spectral-line mode. The number of channels is 4096 for the pulsar backend and 65 536 for the spectral-line backend (wideband mode), corresponding to a frequency coverage from $1000 - 1500$ MHz, which is somewhat broader than the designed bandwidth of the 19-beam receiver ($1050 - 1450$ MHz). The sampling time, i.e., the integration time for raw data, is set to 196.608 μs for the pulsar mode and 1.00663296 s for the spectral-line mode. The intensity for each of the 19 beams is calibrated by the

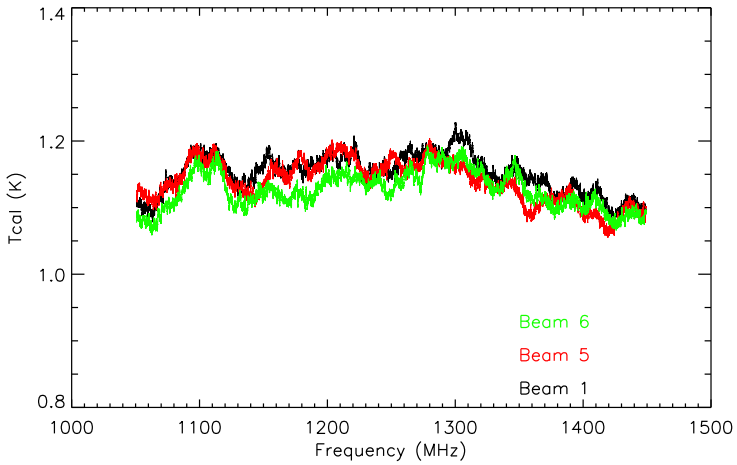

Fig. 1 The low power noise diode temperatures of Beam 1, Beam 5 and Beam 6. The three beams plotted here are representative of the rest. The data for all 19 beams and polarizations are available and are being applied for subsequent calibration.

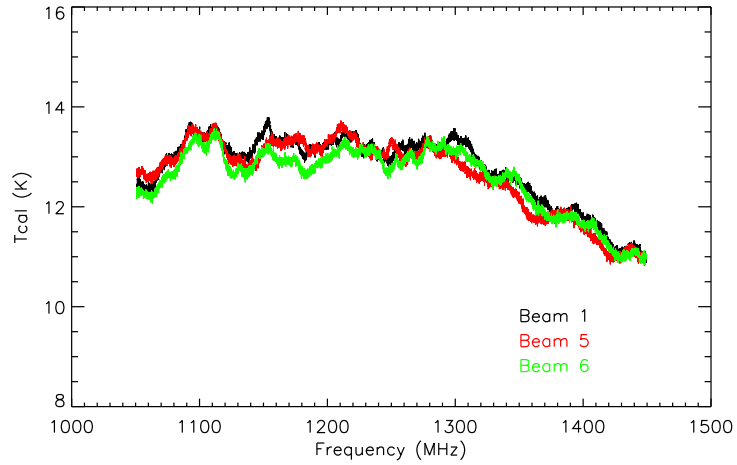

Fig. 2 The high power noise diode temperatures of Beam 1, Beam 5 and Beam 6. The three beams plotted here are representative of the rest. The data for all 19 beams and polarizations are available and are being applied for subsequent calibration.

periodic injection of a high-intensity noise signal ($\sim$10 K, see Sect. 2.1) with a period of 0.2 s.

2.2.2 Data processing procedure

A standard pipeline for processing the mapping data of the 19-beam receiver is still under development. In the following analysis, the mapping data are processed employing IDL. The data recorded by the pulsar backend are adopted, which have dual linear polarizations (XX and YY) and a relatively high time-resolution. We first compress the raw data in the time dimension to have an identical time-resolution with the periodic injected noise. The antenna temperature $T_a(\nu)$ for each of the polarizations is then converted from the raw counts by utilizing the noise diode calibrator. The observed intensity (XX or YY, in K) corresponding to a frequency can be extracted from the spectra after removing the RFI. Together with the data recording time yielded by the backend, one series of pairs of $\{t_{\rm obs}, {\rm intensity}\}$ can be obtained. During the raster scan observation, the phase center of the feed is measured by a real-time measurement system (see Jiang et al. 2019 for a details), which can be converted to the telescope pointing of the central beam (M01) in the horizontal coordinate system (Alt, Az). The telescope pointing in the equatorial coordinates (RA, Dec in J2000) is then calculated from the horizontal coordinates Alt and Az after considering the precession, nutation, aberration and also the refraction effect of the atmosphere. With the time information given by the measurement system, we can derive another series

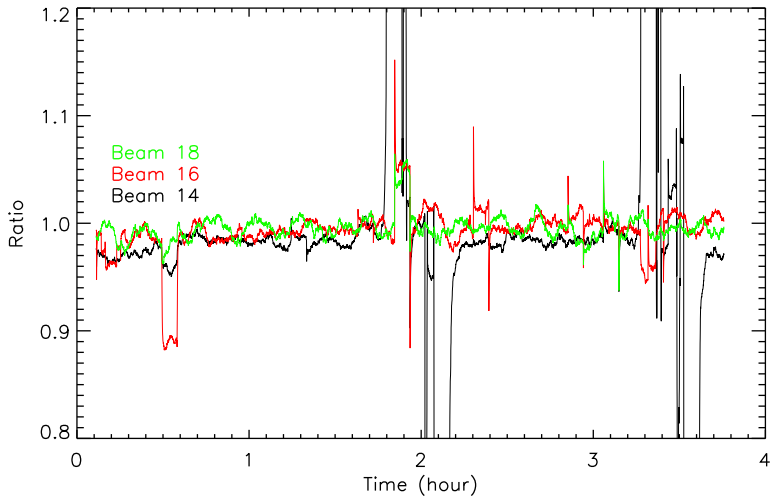

Fig. 3 The electronic gain fluctuations of the system over several hours. The y-axis represents the ratio of fluctuations with respect to the mean temperature over time of Beams 14, 16 and 18. The three beams presented here represent the strongest electronic gain fluctuations out of all 19.

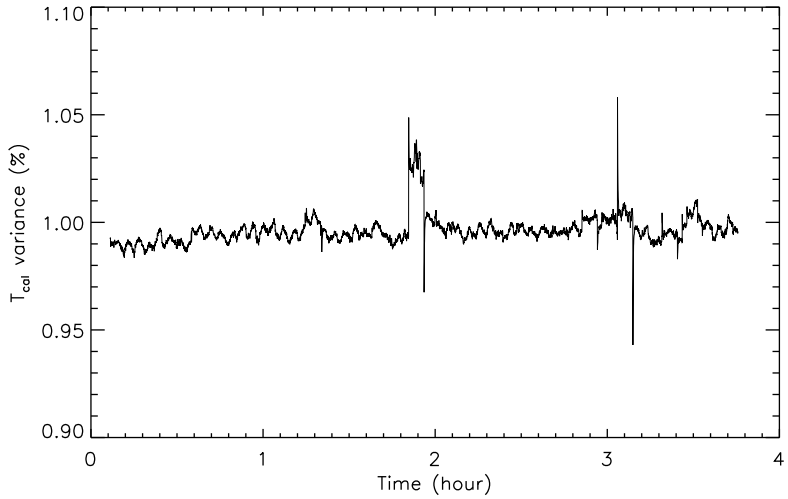

Fig. 4 Stability of the noise diode. An upper limit on the noise diode stability as a function of time measured by monitoring the median value of the electronic gain in all 19 beams during hot load measurements.

of pairs of $\{t_{\rm obs}, {\rm coordinates}\}$. By cross-matching time between the two series of flow data, a data-cube with information on RA, Dec and intensity is derived. Then the data-cube can be regridded to construct the intensity map.

An example of a total intensity map is exhibited in Figure 5. The continuum background is calculated and removed to display the sidelobes and the weak field sources more clearly in the plots on logarithmic-scale. We compare it with the continuum map of the same sky area obtained by the NRAO/VLA Sky Survey (NVSS)[1] at 1.4 GHz, and found that the detected positions of four weak radio sources near RA- and Dec-offsets of ($-9'$,+15′), ($-8'$,+8′), (6.5′, $-16.5'$) and ($-17'$,$-15'$) are consistent. Then, the background radio sources are fitted by two-dimensional (2-D) Gaussian models and removed. A similar procedure for data processing is made to generate the mapping data for other beams, and examples of the results are given in Figure 6. The patterns of beam response depicted in Figure 6 are similar to the radiation patterns yielded by simulations (Smith et al. 2016). According to the angular distance of the beam center to that of the central beam M01, $d_{\rm M01}$, the other 18 elements of the 19-beam receiver are distributed in three concentric ring-shaped areas (see Fig. 7): (1st-ring) M02-M07, with $d_{\rm M01} \sim 5.8$ arcmin; (2nd-ring) M09, M11, M13, M15, M17, M19, with

[1] `https://www.cv.nrao.edu/nvss/postage.shtml`

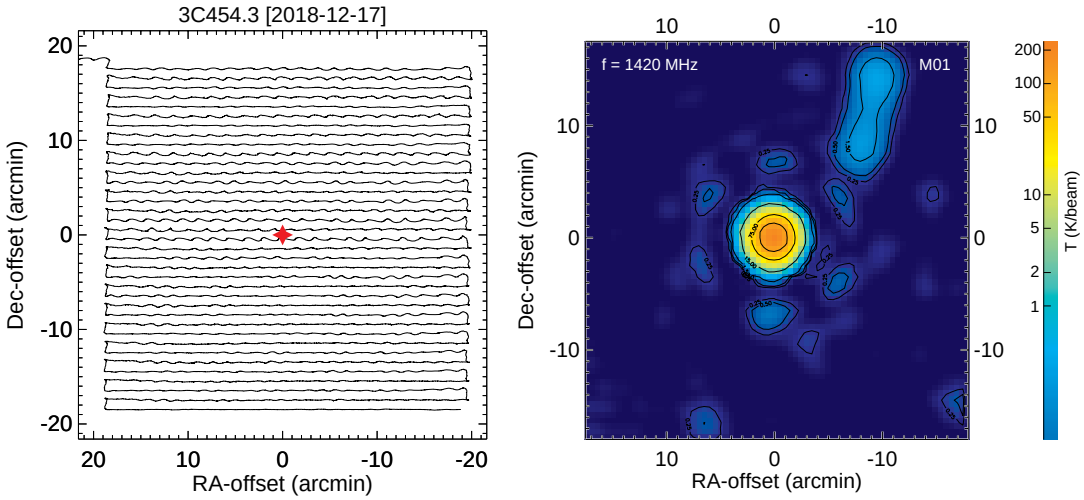

Fig. 5 *Left*: The telescope track for a raster scan along the Dec direction. The covered sky area is $\sim 37' \times 37'$. The target source (3C 454.3) is marked by a red star in the center of the plot. The X- and Y-axes indicate the RA- and Dec-offsets relative to the equatorial coordinates of 3C 454.3 (RA: 22h53m57.7479s, Dec: +16d08m53.561s, in J2000), respectively. *Right*: distribution map of total intensity obtained by the central beam (M01) near the frequency of 1420 MHz. The intensity distributions in a logarithmic-scale are indicated by different colors. The contours signify the intensities with levels of 0.25, 0.5, 1.5, 15, 75 and 150 K.

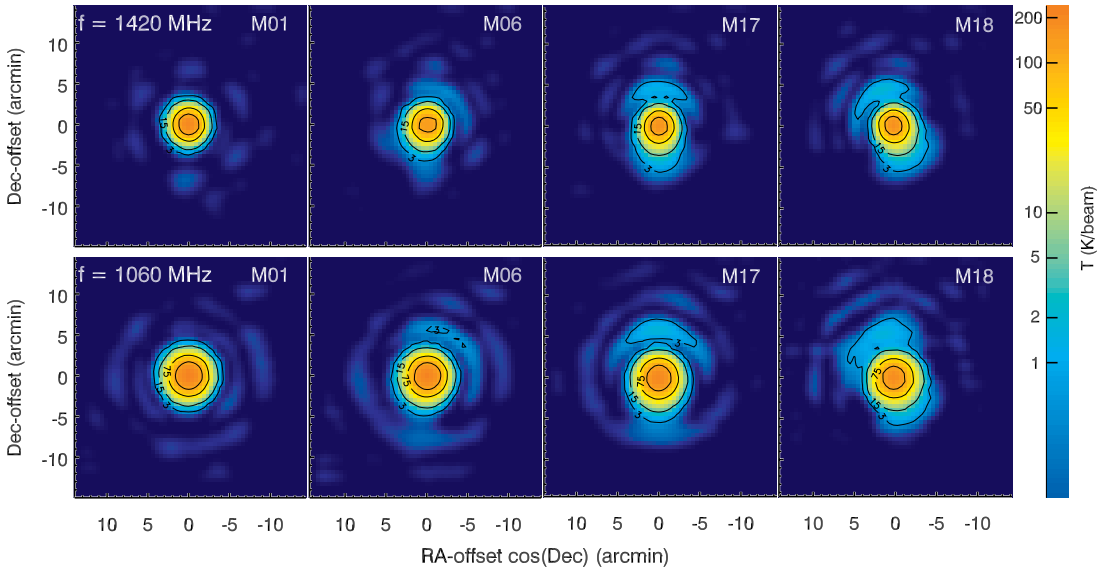

Fig. 6 *Upper panels*: distribution maps of total intensity obtained by raster scan observations of beams M01, M06, M17, and M18 near the frequency of 1420 MHz. *Lower panels*: similar to the upper panels, but for the observation frequency near 1060 MHz. The target source is 3C 454.3. The observation date is 2018 December 17. In each map, the intensity distributions in a logarithmic-scale are indicated by different colors. Contours (*black lines*) signify the intensities with levels of 3, 15, 75 and 150 K. The X- and Y-axes indicate the RA- and Dec-offsets relative to the equatorial coordinates of 3C 454.3. A correction factor cos(Dec) is applied for the X-axis in each of the plots.

$d_{\rm M01} \sim 10.0$ arcmin; (3rd-ring) M08, M10, M12, M14, M16, M18, with $d_{\rm M01} \sim 11.6$ arcmin. With the increase of $d_{\rm M01}$, the sidelobes become more and more significant. The morphology of the sidelobes and their angular distances to the beam center depend on the observation frequency. Other notable features are the noncircular morphology and coma of the main beam, which are negligible for the central beam, but seem to become more and more significant with the increase of $d_{\rm M01}$ for the outer beams.

To fit the main-beam power pattern $P(\theta, \psi)$ with consideration of ellipticity and coma, and determine the combined response of the 19-element multi-beam receiver, we follow the definition of a 'skew Gaussian' given by Heiles et al. (2001). Nine parameters for the i-th beam

Table 1 Parameters of the beam center (X_c, Y_c) for each of the 19 beams (also see Fig. 7), obtained by fitting the observed total intensity maps towards 3C 454.3 observed between 2018 December 07 and December 17.

Scan Direction	(2018–12–07) (Along RA)		(2018–12–08) (Along Dec)		(2018–12–16) (Along RA)		(2018–12–17) (Along Dec)		Mean values	
Beam No.	X_c (′)	Y_c (′)	X_c (′)	Y_c (′)	X_c (′)	Y_c (′)	X_c (′)	Y_c (′)	X_c (′)	Y_c (′)
M01	0.00	0.00	−0.02	0.01	−0.06	−0.05	−0.06	−0.02	−0.04	−0.02
M02	5.81	0.03	5.81	0.03	5.69	−0.05	5.73	−0.04	5.76	−0.01
M03	2.89	−4.97	2.94	−4.93	2.81	−5.06	2.83	−4.99	2.86	−4.98
M04	−2.84	−4.99	−2.81	−5.00	−2.95	−5.03	−2.95	−5.02	−2.89	−5.01
M05	−5.75	−0.03	−5.74	−0.01	−5.82	−0.04	−5.80	0.01	−5.78	−0.02
M06	−2.90	5.00	−2.91	5.00	−2.92	4.94	−2.94	4.97	−2.92	4.98
M07	2.89	5.01	2.85	5.03	2.83	4.90	2.83	4.95	2.85	4.97
M08	11.58	0.01	11.60	0.05	11.49	−0.06	11.53	−0.07	11.55	−0.02
M09	8.67	−4.96	8.74	−4.93	8.56	−5.07	8.64	−5.06	8.65	−5.01
M10	5.81	−9.99	5.89	−9.94	5.69	−10.10	5.70	−10.04	5.78	−10.02
M11	0.08	−9.99	0.13	−9.96	−0.09	−10.05	−0.10	−10.06	0.00	−10.04
M12	−5.69	−10.06	−5.65	−10.10	−5.90	−10.07	−5.90	−10.07	−5.78	−10.07
M13	−8.57	−5.07	−8.60	−5.05	−8.75	−5.05	−8.74	−5.04	−8.67	−5.05
M14	—	—	−11.58	−0.05	—	—	−11.64	0.00	−11.61	−0.02
M15	−8.67	4.93	−8.69	5.00	−8.67	4.96	−8.72	4.99	−8.68	4.99
M16	−5.81	10.01	−5.82	10.05	−5.81	10.00	−5.85	10.02	−5.83	10.02
M17	−0.02	10.01	−0.02	10.03	−0.01	9.95	−0.07	9.99	−0.03	10.00
M18	5.79	10.04	5.77	10.06	5.74	9.94	5.73	9.96	5.76	10.00
M19	8.67	5.01	8.66	5.07	8.58	4.92	8.60	4.94	8.63	4.98

For the central beam M01, $X_c = (RA_{\rm measured} - RA_{\rm source})\cos(Dec)$ and $Y_c = Dec_{\rm measured} - Dec_{\rm source}$ are the pointing errors of FAST in RA and Dec, respectively. For other beams, X_c and Y_c are taken as the angular offsets relative to the true center of beam M01. The mean values of X_c and Y_c for each of the 19 beams are expressed in the last two columns. For beam M14, parameters of the beam center cannot be fitted well from the observation data of 2018 December 07 and December 16, due to a serious scanning effect.

are the peak intensity A_0, beam center X_c and Y_c, the average beamwidth Θ_0, beam ellipticity Θ_1, beam orientation $\phi_{\rm beam}$, coma $\alpha_{\rm coma}$ with orientation $\phi_{\rm coma}$ and a factor ϵ. For the central beam M01, $X_c = (RA_{\rm measured} - RA_{\rm source})\cos(Dec)$ and $Y_c = Dec_{\rm measured} - Dec_{\rm source}$ are the pointing errors of FAST in RA and Dec, respectively. For other beams, the fitting parameters X_c and Y_c are taken as the angular offsets relative to the true center of beam M01. For each beam, the main-beam power pattern is parameterized in polar coordinates (θ, ϕ) as

$$P(\theta,\phi) = A_0 \exp[-\frac{\theta^2(1-\min\{\alpha_{\rm coma}\frac{\theta_{\rm coma}}{\Theta_0},\epsilon\})}{\Theta^2}], \quad (1)$$

where $\theta_{\rm coma} = \theta\cos(\phi-\phi_{\rm coma})$ and $\Theta = \Theta_0 + \Theta_1\cos 2(\phi-\phi_{\rm beam})$. Here, θ is the angular distance of the position to the true beam center, ϕ is the position angle in equatorial coordinates (RA, Dec in J2000) and defined to be zero along the positive RA-offset axis and increases towards positive Dec-offset axis. Following Heiles et al. (2001), we also take ϵ as a constant parameter 0.75 during the fit. Together with the term $\min\{\alpha_{\rm coma}\frac{\theta_{\rm coma}}{\Theta_0},\epsilon\}$, they are used to prevent the coma term from unduly distorting the beam far from the beam center (Heiles et al. 2001). The MPFIT package[2] is adopted to perform the minimization. In the following, we give a general discussion about the combined beam response, the beamwidth and also the pointing errors of FAST, obtained by fitting the observed total intensity (XX+YY) maps.

[2] `http://www.physics.wisc.edu/~craigm/idl/fitting.html`

2.2.3 The convolved beam pattern of the 19-beam receiver

To measure the beam properties, we analyzed the mapping data toward 3C 454.3, which is the strongest source at 1.4 GHz among the observed $37' \times 37'$ targets (1902+319, 1859+129, 3C 454.3, 2023+318, etc) by FAST. Raster scans covering a sky area of $\sim 37' \times 37'$ were conducted four times along RA or Dec directions. The fitted parameters of the beam center for each of the 19 beams are listed in Table 1. With the fitted beam center, we combine the intensity distribution maps derived by each of the 19 beams to yield a composite response of the 19-beam receiver as illustrated in Figure 7. The observed layout of the 19-beam receiver is consistent with the schematic diagram provided by Dunning et al. (2017) and Li et al. (2018). Around the main beams, the responses of first sidelobes for the 12 outer beams (M08-M19) are also visible in the logarithmic-scale plot. Similar results were obtained by analyzing the observation data toward other sources, e.g., 3C 380 and 2023+318.

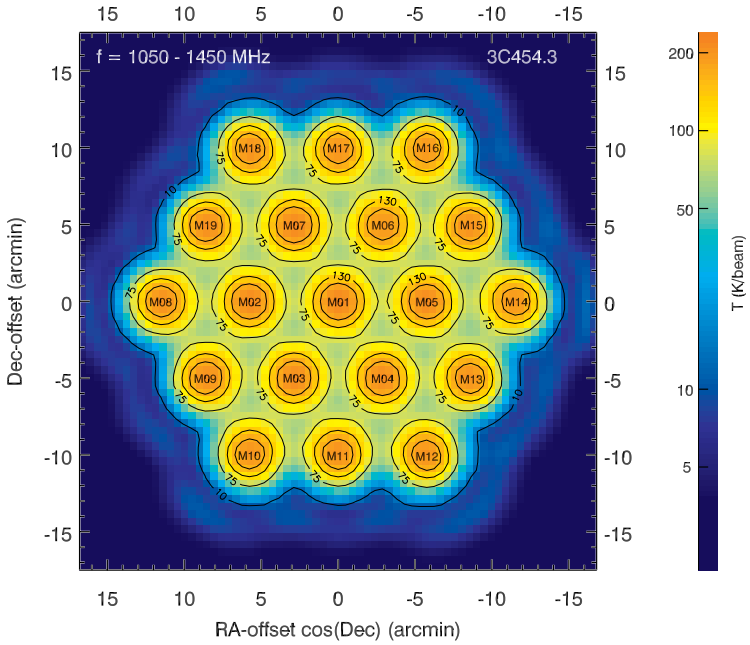

Fig. 7 Combined response of the 19-beam receiver of FAST. The target object is 3C 454.3. The frequency coverage used to infer the total intensity is from 1050 MHz to 1450 MHz. The intensity distributions in a logarithmic-scale are indicated by different colors. Contours (*black lines*) signify the intensities with levels of 10, 75, 130 and 175 K. The X- and Y-axes indicate the RA- and Dec-offsets relative to the center of beam M01 (see Table 1). The numbering of the 19 beams (M01–M19) is marked in the plot.

It is necessary to emphasize that the intensity distributions exhibited in Figure 6 and Figure 7 are the beam response to the point source 3C 454.3 versus the angular offsets. They are the convolution of the beam pattern with the brightness distribution on the sky.

2.2.4 Beamwidth

The half-power beamwidth (HPBW) is related to the average beamwidth Θ_0 by HPBW $= 2(\ln 2)^{1/2}\Theta_0$. Here, Θ_0 is derived by fitting the total intensity distribution maps with a 'skew Gaussian' model as written in Equation (1). The HPBW as a function of the observation frequency for the 19 beams is depicted in Figure 8. In comparison to the central beam, the outer beams tend to have larger beamwidths, with a difference of no more than 0.2 arcmin. The HPBW decreases with the increase of frequency. As discussed in Jiang et al. (2019), the theoretical HPBW of a telescope with diameter D is HPBW $= 1.02\lambda/D$ for a uniformly illuminated aperture and HPBW $= 1.22\lambda/D$ for a cosine-tapered illuminated aperture. Here, a diameter of $D = 300$ m is assumed. As demonstrated in Figure 8, the fitted beamwidths of the 19-beam receiver fall within the two theoretical curves of HPBW versus frequency, but with a less steep slope than that of a standard λ/D proportionality.

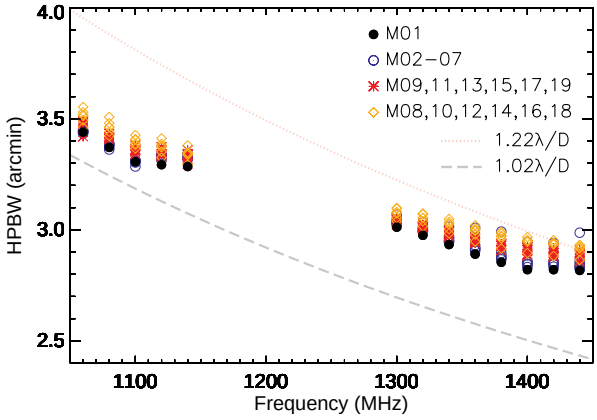

Fig. 8 HPBW versus observation frequency for the 19-beam receiver of FAST. The target source is 3C 454.3. The observation date is 2018 December 17. The beamwidths corresponding to the frequency range of 1160−1280 MHz cannot be fitted well, as strong RFI appears during the observation.

2.2.5 Pointing errors

As discussed in Jiang et al. (2019), the analysis of pointing errors can be used to evaluate the pointing accuracy, improve the pointing of the telescope, and also guide the error analysis of observations. Systematic observations have been made to measure the pointing errors of FAST by raster scan observations. As we only care about the pointing errors of the central beam M01, the mapping area to-

Table 2 HPBW of the 19-beam receiver of FAST for different observation frequencies, which are used for the plot displayed in Fig. 8.

Beam No.	Frequency (MHz)												
	1060	1080	1100	1120	1140	1300	1320	1340	1360	1380	1400	1420	1440
M01	3.44′	3.37′	3.31′	3.29′	3.29′	3.01′	2.98′	2.93′	2.89′	2.85′	2.82′	2.82′	2.82′
M02	3.44′	3.37′	3.31′	3.33′	3.33′	3.04′	3.00′	2.96′	2.92′	2.88′	2.85′	2.85′	2.84′
M03	3.44′	3.38′	3.30′	3.33′	3.32′	3.03′	3.00′	2.95′	2.91′	2.87′	2.84′	2.84′	2.83′
M04	3.44′	3.38′	3.31′	3.34′	3.32′	3.05′	3.01′	2.97′	2.93′	2.90′	2.86′	2.86′	2.85′
M05	3.43′	3.36′	3.29′	3.31′	3.32′	3.03′	2.99′	2.95′	2.91′	2.87′	2.83′	2.83′	2.82′
M06	3.44′	3.39′	3.31′	3.34′	3.34′	3.07′	3.03′	3.01′	3.01′	2.99′	2.95′	2.94′	2.99′
M07	3.45′	3.39′	3.31′	3.33′	3.34′	3.02′	2.99′	2.95′	2.92′	2.88′	2.86′	2.86′	2.86′
M08	3.46′	3.42′	3.38′	3.35′	3.34′	3.04′	3.02′	2.98′	2.95′	2.92′	2.90′	2.88′	2.86′
M09	3.48′	3.41′	3.36′	3.33′	3.30′	3.04′	3.01′	2.97′	2.94′	2.91′	2.88′	2.88′	2.86′
M10	3.52′	3.46′	3.40′	3.38′	3.35′	3.08′	3.05′	3.03′	3.00′	2.97′	2.95′	2.94′	2.92′
M11	3.49′	3.43′	3.38′	3.37′	3.34′	3.05′	3.02′	3.00′	2.97′	2.94′	2.92′	2.91′	2.90′
M12	3.49′	3.44′	3.39′	3.37′	3.34′	3.07′	3.05′	3.03′	3.00′	2.97′	2.95′	2.94′	2.90′
M13	3.48′	3.41′	3.34′	3.33′	3.32′	3.04′	3.01′	2.98′	2.95′	2.93′	2.91′	2.91′	2.89′
M14	3.53′	3.48′	3.43′	3.41′	3.38′	3.10′	3.07′	3.04′	3.01′	2.98′	2.95′	2.94′	2.92′
M15	3.49′	3.42′	3.36′	3.36′	3.36′	3.06′	3.01′	2.98′	2.94′	2.91′	2.89′	2.88′	2.86′
M16	3.51′	3.46′	3.41′	3.39′	3.34′	3.10′	3.07′	3.05′	3.02′	2.99′	2.97′	2.95′	2.93′
M17	3.49′	3.42′	3.35′	3.34′	3.33′	3.02′	3.00′	2.99′	2.97′	2.94′	2.92′	2.92′	2.91′
M18	3.55′	3.51′	3.37′	3.33′	3.29′	3.05′	3.04′	3.00′	2.98′	2.96′	2.95′	2.94′	2.93′
M19	3.42′	3.41′	3.36′	3.33′	3.34′	3.03′	3.00′	2.98′	2.95′	2.93′	2.91′	2.90′	2.89′

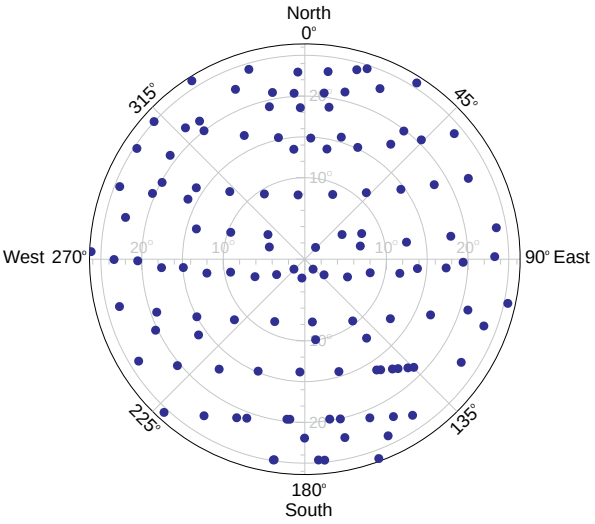

Fig. 9 Distributions of the observed pointing calibrators in the sky coverage of FAST with full gain (ZA $\lesssim 26.4°$). The observation period is from 2019 February 16 to March 15. In this plot, the ZA is from $0°$ to $26.4°$ as indicated by grey circles, and the azimuth angle is from $0°$ to $360°$. The directions marked in the periphery of the plot are geographic north, east, south and west at the FAST site.

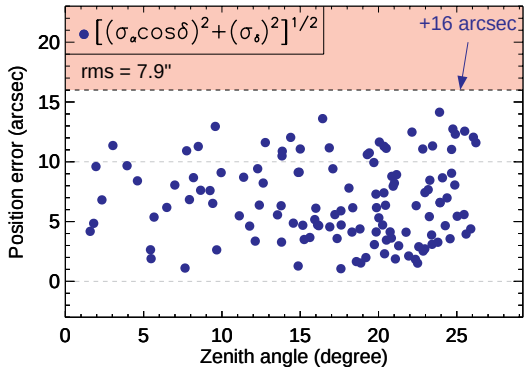

Fig. 10 Pointing error $[(\sigma_\alpha \cos\delta)^2+(\sigma_\delta)^2]^{1/2}$ versus ZA for the 19-beam receiver of FAST.

ward a target source is set to $\sim 7' \times 7'$. About 7 minutes are needed to acquire such a map with subscan separation of $1'$. The target sources are selected from the catalog of pointing calibrators published by Condon & Yin (2001), which contains 3399 strong and compact radio sources with accurate positions from the NVSS, and uniformly covering the sky north of $\delta = -40°$ (J2000). The dataset applied in the analysis was observed from 2019 February 16 to March 15, which include 126 raster scan observations along RA or Dec directions. As demonstrated in Figure 9, the observed pointing calibrators are distributed widely in the sky coverage of FAST with full gain (zenith angle (ZA) $\lesssim 26.4°$).

The observation data are processed in a similar procedure as described in Sect. 2.2.2. To fit the pointing errors in RA and Dec directions, a 2-D Gaussian model is adopted, which is good enough as the central beam does not present significant beam ellipticity and coma feature (Figs. 5 and 6). The pointing errors $[(\sigma_\alpha\cos\delta)^2+(\sigma_\delta)^2]^{1/2}$ are typically smaller than $16''$ as shown in Figure 10. The root mean square (RMS) of pointing errors is $7.9''$, which is less than one-tenth of the beamwidth near 1450 MHz (beamwidth$_{1450}$/10 $\sim 2.8'/10 = 16.8''$).

2.3 Aperture Efficiency and System Temperature

Aperture efficiency (η) and system temperature ($T_{\rm sys}$) are two basic parameters of FAST. Both of them are expected to vary as a function of ZA ($\theta_{\rm ZA}$) and frequency. The 19 beams are divided into four categories according to separation from the central beam. The four categories are : (1) Beam 1; (2) Beams 2, 3, 4, 5, 6, and 7; (3) Beams 8, 10, 12, 14, 16, and 18; (4) Beams 9, 11, 13, 15, 17 and 19. Though the performance of aperture efficiency and system temperature in each category is expected to be the same, asymmetry of the receiver platform may lead to deviation. Thus we obtained the measurements toward all 19 beams.

The aperture efficiency curve was obtained by repeating observations of the calibrator 3C 286 and its off position at different ZAs. The position switch mode that is introduced in Section 4 was adopted. This mode provides quick switch between ON and OFF source positions. The separation between ON and OFF position was selected to allow for measuring the aperture efficiency curve of two beams (e.g, Beams 1 and 19) simultaneously, which increases measurement efficiency.

Observations of Beams 1, 2, 8, and 19 were acquired during 2019 August 7 and 2019 August 24. To make it clear, we take the aperture efficiency measurement of Beams 1 and 19 as an example. At first, the telescope tracked the calibrator 3C 286 with Beam 1 (source ON for Beam 1, source OFF position for Beam 19) for 90 s, and then switched to the sky position with offset of ($-8.85'$, $-5.11'$). At this position, the calibrator 3C 286 was OFF for Beam 1 but lay in Beam 19. After tracking for 90 s, the telescope switched back to track 3C 286 with Beam 1. A cycle consisted of one ON and one OFF phase for each beam. A total of 90 cycles was recorded during the available tracking time of $\sim$ 6 hours for 3C 286. Supplementary measurements of the aperture efficiency curve for the other 15 beams were taken by tracking 3C 286 during 2019 December 19 and 2019 December 25. During these observations, the total tracking time in a cycle was reduced to 60 s, including 30 s for both source on and source off. A total of 85 cycles over $\sim$ 3 hr was taken for measurement of both beams.

The system temperature curve of 19 beams was obtained by continuously tracking a clean sky position (α_{2000}=23$^{\rm h}$30$^{\rm m}$0$^{\rm s}$.0, δ_{2000}=25°39′10.6″) from rise to set on 2019 September 14.

In the above measurements, spectral backend with sampling time of 1.00663296 s and channel width of 7.62939 kHz was adopted to record the data. The high noise signal ($\sim$ 11 K) was injected at a synchronized period of 2.01326592 s. The duration time of cal on and cal off was 1.00663296 s. During calculation, channel width of the data was smoothed to 1 MHz. The aperture efficiency was derived for each observation cycle while the system temperature was derived for each sampling time.

2.3.1 Aperture efficiency

Based on absolute measurement of noise dipole in Section 2.1, the observed data were calibrated to antenna temperature T_A in K. The antenna temperature of 3C 286, $T_A^{\rm 3C\ 286}$ was derived by the difference between source ON and source OFF data for each beam.

3C 286 is a stable flux calibrator. The frequency dependency of the spectral flux density of 3C 286 could be fitted with a polynomial function (Perley & Butler 2017),

$$\log(S) = a_0 + a_1\log(\nu_G) + a_2[\log(\nu_G)]^2 + a_3[\log(\nu_G)]^3, \quad (2)$$

where S and ν_G are the spectral flux density in Jy and the frequency respectively. We adopted the values of $a_0 = 1.2481$, $a_1 = -0.4507$, $a_2 = -0.1798$ and $a_3 = 0.0357$ that are valid for 3C 286 at frequency range of [0.05–50] GHz (Perley & Butler 2017).

Measured gain (G) of FAST is expressed as $G_0 = A_{\rm eff}/2k$, in which $A_{\rm eff}$ is the effective illumination area. In observation, G is calculated by the ratio between antenna temperature and flux density, $G = T_A^{\rm 3C\ 286}/S_A^{\rm 3C\ 286}$. The prefect gain G_0 of FAST is $G_0 = A_{\rm geo}/2k$ for single polarization, in which $A_{\rm geo}$ and k are geometric illumination area and Boltzmann constant respectively. The geometric illumination area with diameter of 300 m leads to G_0= 25.6 K Jy^{-1} for FAST.

The aperture efficiency η of FAST is derived by,

$$\eta = G/G_0 = A_{\rm eff}/A_{\rm geo} = \frac{2kT_A^{\rm 3C\ 286}}{A_{\rm geo}S_A^{\rm 3C\ 286}}. \quad (3)$$

For the FAST system, η is contributed by six main components:

1. $\eta_{\rm sf}$, reflection efficiency of the main reflector. It is described by the Ruze equation, $\eta_{\rm sf} = e^{-(\frac{4\pi\varepsilon}{\lambda})^2}$, in which ε and λ are RMS of the surface error and observational wavelength, respectively. The RMS of the surface error is contributed by controlling accuracy of panels, which is $\sim$ 5 mm at 21 cm (Jiang et al. 2019). This results in $\eta_{\rm sf}$ of $\sim$ 91%.
2. $\eta_{\rm bl}$, the efficiency when the shielding of the feed cabin is considered. The diameter of the feed cabin of $\sim$ 10 m leads to $\eta_{\rm bl}$ value of 99.9%.

3. $\eta_{\rm s}$, spillover efficiency.
4. $\eta_{\rm t}$, illumination efficiency of the feed. It equals 76% when a -13 dB Gaussian illumination is adopted (Jiang et al. 2019).
5. $\eta_{\rm misc}$, efficiency of other aspects including the offset of the feed phase, matching loss of feed.
6. $\eta_{\rm sloss}$, the percent of effective surface area compared to a 300-m diameter paraboloid. The value is 1 when $\theta_{\rm ZA}$ is less than 26.4°. When $\theta_{\rm ZA}$ is greater than 26.4°, the reflection area decreases. $\eta_{\rm sloss}$ would decrease and reach $\sim$ 2/3 when $\theta_{\rm ZA} = 40°$.

The aperture efficiency is a synthetical result of the above effects and is described by the following equation,

$$\eta = \eta_{\rm sf} \cdot \eta_{\rm bl} \cdot \eta_{\rm s} \cdot \eta_{\rm t} \cdot \eta_{\rm misc} \cdot \eta_{\rm sloss} \,. \quad (4)$$

The values of $\eta_{\rm sf}$, $\eta_{\rm bl}$, $\eta_{\rm s}$, $\eta_{\rm t}$ and $\eta_{\rm misc}$ are almost constant. The value of η is mainly determined by $\eta_{\rm sloss}$. As plotted in Figure 11, the value η at all frequencies would stay almost constant when $\theta_{\rm ZA}$ is less than 26.4° and decreases linearly when $\theta_{\rm ZA} > 26.4°$. This is consistent with the fact that FAST would lose part of the reflection panels when $\theta_{\rm ZA} > 26.4°$.

We fitted variation of η as a function of $\theta_{\rm ZA}$ at a specific frequency with two linear equations. The formula is written as follows,

$$\eta = \begin{cases} a\,\theta_{\rm ZA} + {\rm b},\ 0° \le \theta_{\rm ZA} \le 26.4° \\ c\,\theta_{\rm ZA} + {\rm d},\ 26.4° < \theta_{\rm ZA} \le 40°. \end{cases} \quad (5)$$

Here d satisfies the equation $d = b + 26.4(a - c)$. The fitting results of parameters a, b and c for different frequencies are expressed in Table 3. As an example, the fitting results of η for Beams 1, 2, 8 and 19 are shown in Figure 11. The fitting results of the other 15 beams are depicted in Figure B.1.

The gain of FAST could be expressed with $G = \eta G_0$, in which G_0 = 25.6 K Jy^{-1}. Flux density (in unit of Jy) of a point source is converted from antenna temperature by dividing the gain value. The averaged gain values of 19 beams within ZA of 26.4° are listed in Table 5. Beam 16 has the smallest gain value among 19 beams. The gain ratio of Beam 16 compared to Beam 1 reaches 0.83 ± 0.02 at 1400 and 1450 MHz.

2.3.2 System temperature

Observation of sky position (α_{2000}=23$^{\rm h}$30$^{\rm m}$0$^{\rm s}$.0, δ_{2000}=25°39′10.6″) allows us to measure system temperature from ZA of 40° to nearly 0°. The data were calibrated to antenna temperature in K with noise curve. For a single dish telescope at L band, $T_{\rm sys}$ consists of four main sources (Campbell 2002):

1. Noise contribution from receiver, $T_{\rm rec}$. For the 19 beam receiver of FAST, it is measured as 7–9 K, including $\sim$ 4 K from low noise amplifier (LAN) (see section 4.1.1 in Jiang et al. 2019 for details).
2. Continuum brightness temperature of the sky, $T_{\rm sky}$. This includes 2.73 K from cosmic microwave background (CMB) and non-thermal emission from the Milky Way. The value of $T_{\rm sky}$ at 1.4 GHz is $\sim$ 3.48 K toward position (α_{2000}=23$^{\rm h}$30$^{\rm m}$0$^{\rm s}$.0, δ_{2000}=25°39′10.6″) (CHIPASS survey; Calabretta et al. 2014).
3. Emission from the Earth's atmosphere $T_{\rm atm}$. This value should be within a few K.
4. Radiation from the surrounding terrain, $T_{\rm scat}$. This contribution originates from the side lobe of FAST. Unlike other single dish facilities with fixed surface and horn, the illumination area of the horn varies for different ZAs, leading to different values of $T_{\rm scat}$.

System temperature is the synthetical result of the above components.

$$T_{\rm sys} = T_{\rm rec} + T_{\rm sky} + T_{\rm atm} + T_{\rm scat} \,. \quad (6)$$

The variation of system temperature $T_{\rm sys}$ as a function of ZA can be fitted with the following formula,

$$T_{\rm sys} = {\rm P}_0 \arctan(\sqrt{1 + \theta_{\rm ZA}{}^{\rm n}} - {\rm P}_1) + {\rm P}_2, \quad (7)$$

which is valid for $0° \le \theta_{\rm ZA} <= 40°$. The values of P_0, P_1, P_2 and n in different frequencies are shown in Table 4. An example of fitting the $T_{\rm sys}$ curve is plotted in Figure 12. The results for the other beams are depicted in Figure C.1.

A significant feature in the $T_{\rm sys}$ profile is that the $T_{\rm sys}$ value of most beams reaches its minimum at ZA range of [10°,15°]. When ZA is smaller than 10°, the $T_{\rm sys}$ value would increase by a maximum value of 1 K. Though the central hole of the spherical surface was shielded with metal mesh during observations, the leakage of ground emission ($\sim$ 300 K) from the central hole goes into the main beam and contributes $T_{\rm sys}$ increase when ZA is less than 10°. When ZA becomes larger than 15°, the $T_{\rm sys}$ value increases by 5–7 K, which arises from emission of a nearby mountain through the sidelobe.

2.3.3 Discussion

The observations lie in $\theta_{\rm ZA}$ range of [4.9,40] deg for the η curve. The fitting results are expected to be valid for $\theta_{\rm ZA}$ range of [0,40] degree for the following reason. When $\theta_{\rm ZA} < 4.9°$, there is no loss of panel coverage. In this case, η should stay almost constant as demonstrated by the fitting curves.

Table 3 Details of Fitting Parameters of Aperture Efficiency for all 19 Beams

Beam	Paras	Freq (MHz)								
		1050	1100	1150	1200	1250	1300	1350	1400	1450
M01	a/1e-4	3.31 ± 2.23	2.54 ± 1.85	0.34 ± 1.83	5.03 ± 2.03	4.94 ± 2.02	9.83 ± 1.85	8.50 ± 1.93	7.87 ± 1.95	10.64 ± 1.90
M01	b/1e-1	6.19 ± 0.04	6.32 ± 0.03	6.43 ± 0.03	6.22 ± 0.03	6.22 ± 0.03	6.08 ± 0.03	6.12 ± 0.03	6.14 ± 0.03	5.98 ± 0.03
M01	c/1e-2	–1.58 ± 0.02	–1.61 ± 0.03	–1.37 ± 0.04	–1.40 ± 0.04	–1.42 ± 0.03	–1.38 ± 0.03	–1.40 ± 0.02	–1.34 ± 0.02	–1.26 ± 0.02
M02	a/1e-4	9.46 ± 3.53	6.28 ± 3.09	9.01 ± 3.14	12.13 ± 3.12	10.98 ± 3.06	11.31 ± 2.16	8.71 ± 2.09	8.78 ± 2.06	13.07 ± 1.98
M02	b/1e-1	5.97 ± 0.06	5.97 ± 0.05	5.99 ± 0.05	5.81 ± 0.05	5.81 ± 0.05	5.65 ± 0.04	5.75 ± 0.03	5.75 ± 0.03	5.62 ± 0.03
M02	c/1e-2	–1.54 ± 0.03	–1.62 ± 0.03	–1.46 ± 0.03	–1.44 ± 0.02	–1.42 ± 0.02	–1.29 ± 0.02	–1.32 ± 0.02	–1.33 ± 0.02	–1.21 ± 0.02
M03	a/1e-4	1.79 ± 4.21	4.39 ± 3.55	2.41 ± 4.46	5.95 ± 4.69	6.90 ± 3.21	7.41 ± 2.60	9.99 ± 2.63	7.66 ± 2.60	10.30 ± 2.72
M03	b/1e-1	6.41 ± 0.07	6.24 ± 0.06	6.42 ± 0.07	6.21 ± 0.07	6.17 ± 0.05	6.07 ± 0.04	5.91 ± 0.04	5.99 ± 0.04	5.86 ± 0.04
M03	c/1e-2	–1.70 ± 0.03	–1.80 ± 0.03	–1.56 ± 0.03	–1.63 ± 0.02	–1.59 ± 0.02	–1.56 ± 0.02	-1.53 ± 0.02	–1.47 ± 0.02	–1.35 ± 0.03
M04	a/1e-4	3.57 ± 4.76	1.87 ± 4.08	3.82 ± 3.93	3.90 ± 4.60	8.46 ± 4.65	4.29 ± 3.22	2.75 ± 3.28	1.85 ± 3.26	5.10 ± 3.20
M04	b/1e-1	6.24 ± 0.08	6.15 ± 0.07	6.25 ± 0.06	6.05 ± 0.08	5.98 ± 0.08	5.92 ± 0.05	5.89 ± 0.05	5.89 ± 0.05	5.75 ± 0.05
M04	c/1e-2	–1.80 ± 0.03	–1.82 ± 0.03	–1.65 ± 0.02	–1.57 ± 0.06	–1.58 ± 0.02	–1.42 ± 0.02	–1.45 ± 0.02	–1.36 ± 0.02	–1.24 ± 0.02
M05	a/1e-4	–3.97 ± 2.87	–4.25 ± 2.72	–4.44 ± 2.72	–7.54 ± 3.48	–4.09 ± 4.19	–5.41 ± 2.35	–3.33 ± 2.26	-4.51 ± 2.42	-4.58 ± 2.53
M05	b/1e-1	6.45 ± 0.05	6.48 ± 0.04	6.68 ± 0.04	6.42 ± 0.06	6.39 ± 0.07	6.26 ± 0.04	6.10 ± 0.04	6.17 ± 0.04	6.11 ± 0.04
M05	c/1e-2	–1.82 ± 0.03	–1.86 ± 0.03	–1.72 ± 0.03	–1.56 ± 0.03	–1.60 ± 0.03	–1.53 ± 0.02	–1.45 ± 0.03	–1.44 ± 0.03	–1.30 ± 0.03
M06	a/1e-4	1.69 ± 2.84	0.74 ± 2.59	-0.00 ± 4.17	1.06 ± 5.18	0.97 ± 3.49	0.33 ± 1.82	3.11 ± 1.80	–0.03 ± 1.76	1.37 ± 1.76
M06	b/1e-1	6.16 ± 0.04	6.22 ± 0.04	6.33 ± 0.07	6.01 ± 0.08	6.04 ± 0.06	5.92 ± 0.03	5.83 ± 0.03	5.89 ± 0.03	5.75 ± 0.03
M06	c/1e-2	–1.74 ± 0.03	–1.80 ± 0.03	–1.60 ± 0.03	–1.50 ± 0.04	–1.44 ± 0.03	–1.33 ± 0.02	–1.38 ± 0.02	-1.35 ± 0.02	–1.22 ± 0.02
M07	a/1e-4	1.71 ± 2.43	0.08 ± 2.18	0.77 ± 2.41	2.03 ± 3.25	2.24 ± 3.64	3.46 ± 1.82	5.46 ± 1.60	6.70 ± 1.65	6.91 ± 1.49
M07	b/1e-1	6.10 ± 0.04	6.04 ± 0.04	6.18 ± 0.04	5.90 ± 0.05	6.02 ± 0.06	5.86 ± 0.03	5.77 ± 0.03	5.73 ± 0.03	5.62 ± 0.02
M07	c/1e-2	–1.68 ± 0.02	–1.64 ± 0.02	–1.52 ± 0.02	–1.39 ± 0.02	–1.43 ± 0.02	–1.32 ± 0.02	–1.34 ± 0.02	–1.36 ± 0.02	–1.22 ± 0.02
M08	a/1e-4	13.91 ± 3.13	17.00 ± 2.98	14.04 ± 3.81	16.81 ± 4.98	17.71 ± 2.95	17.29 ± 2.75	16.95 ± 2.29	15.92 ± 2.31	17.76 ± 2.43
M08	b/1e-1	5.76 ± 0.05	5.75 ± 0.05	5.81 ± 0.06	5.62 ± 0.08	5.54 ± 0.05	5.46 ± 0.04	5.41 ± 0.04	5.34 ± 0.04	5.22 ± 0.04
M08	c/1e-2	–1.60 ± 0.06	-1.70 ± 0.05	–1.52 ± 0.06	–1.50 ± 0.06	–1.50 ± 0.05	–1.47 ± 0.05	-1.45 ± 0.05	–1.37 ± 0.05	–1.28 ± 0.05
M09	a/1e-4	–1.26 ± 2.03	–0.43 ± 1.99	–2.68 ± 1.94	0.12 ± 1.67	0.96 ± 1.60	1.53 ± 1.53	1.09 ± 1.36	1.00 ± 1.11	0.27 ± 0.91
M09	b/1e-1	5.96 ± 0.03	5.95 ± 0.03	5.98 ± 0.03	5.75 ± 0.03	5.77 ± 0.03	5.74 ± 0.02	5.64 ± 0.02	5.57 ± 0.02	5.53 ± 0.02
M09	c/1e-2	–1.39 ± 0.04	–1.43 ± 0.03	–1.28 ± 0.04	–1.24 ± 0.04	–1.24 ± 0.03	–1.18 ± 0.04	–1.09 ± 0.04	–1.06 ± 0.03	–1.01 ± 0.03
M10	a/1e-4	14.36 ± 3.80	15.37 ± 3.39	15.65 ± 3.78	15.20 ± 4.85	18.06 ± 2.92	17.97 ± 2.67	19.34 ± 2.49	16.72 ± 2.52	18.57 ± 2.65
M10	b/1e-1	6.01 ± 0.06	5.98 ± 0.05	6.04 ± 0.06	5.81 ± 0.08	5.86 ± 0.05	5.75 ± 0.04	5.72 ± 0.04	5.69 ± 0.04	5.60 ± 0.04
M10	c/1e-2	–1.79 ± 0.04	–1.83 ± 0.04	-1.74 ± 0.03	–1.73 ± 0.03	–1.78 ± 0.03	–1.74 ± 0.03	–1.72 ± 0.03	–1.66 ± 0.03	–1.58 ± 0.03
M11	a/1e-4	7.68 ± 5.51	2.98 ± 4.73	4.16 ± 4.57	3.38 ± 6.44	2.45 ± 4.86	4.27 ± 3.39	5.99 ± 3.36	5.03 ± 3.28	8.23 ± 3.05
M11	b/1e-1	5.90 ± 0.09	5.94 ± 0.08	6.00 ± 0.07	5.81 ± 0.10	5.80 ± 0.08	5.67 ± 0.06	5.66 ± 0.05	5.61 ± 0.05	5.45 ± 0.05
M11	c/1e-2	–1.59 ± 0.04	-1.59 ± 0.03	–1.55 ± 0.03	–1.35 ± 0.05	–1.36 ± 0.03	–1.31 ± 0.03	–1.35 ± 0.02	–1.27 ± 0.02	–1.18 ± 0.02
M12	a/1e-4	–3.00 ± 5.82	–2.08 ± 4.75	1.33 ± 4.29	4.98 ± 5.10	8.50 ± 4.02	-0.98 ± 3.17	2.94 ± 3.06	2.49 ± 2.71	2.77 ± 2.60
M12	b/1e-1	6.06 ± 0.09	5.96 ± 0.08	5.91 ± 0.07	5.82 ± 0.08	5.76 ± 0.06	5.70 ± 0.05	5.58 ± 0.05	5.53 ± 0.04	5.48 ± 0.04
M12	c/1e-2	–1.56 ± 0.05	–1.49 ± 0.04	–1.45 ± 0.05	–1.56 ± 0.05	-1.69 ± 0.03	–1.35 ± 0.04	-1.40 ± 0.03	–1.34 ± 0.03	-1.27 ± 0.03
M13	a/1e-4	–1.33 ± 4.57	0.41 ± 4.05	2.41 ± 4.07	–1.35 ± 4.89	2.44 ± 3.87	2.60 ± 3.22	4.14 ± 3.11	5.50 ± 2.95	5.83 ± 2.77
M13	b/1e-1	6.18 ± 0.08	6.12 ± 0.07	6.22 ± 0.07	6.23 ± 0.08	6.04 ± 0.06	6.00 ± 0.05	5.94 ± 0.05	5.85 ± 0.05	5.71 ± 0.05
M13	c/1e-2	–1.49 ± 0.04	–1.59 ± 0.03	–1.53 ± 0.04	–1.54 ± 0.07	–1.54 ± 0.03	–1.57 ± 0.02	–1.59 ± 0.03	-1.53 ± 0.03	–1.44 ± 0.03
M14	a/1e-4	0.35 ± 3.81	–0.57 ± 3.77	4.27 ± 3.61	3.01 ± 4.84	7.37 ± 4.78	2.58 ± 2.61	4.43 ± 2.19	5.43 ± 2.22	5.53 ± 2.19
M14	b/1e-1	5.91 ± 0.06	5.98 ± 0.06	5.91 ± 0.06	5.76 ± 0.08	5.73 ± 0.08	5.78 ± 0.04	5.64 ± 0.04	5.59 ± 0.04	5.53 ± 0.04
M14	c/1e-2	–1.56 ± 0.04	–1.67 ± 0.04	–1.65 ± 0.04	–1.57 ± 0.04	–1.64 ± 0.03	–1.68 ± 0.02	–1.61 ± 0.03	–1.60 ± 0.04	–1.51 ± 0.04
M15	a/1e-4	1.33 ± 2.89	-0.59 ± 2.55	–3.57 ± 3.01	3.71 ± 5.82	–1.46 ± 2.36	–2.34 ± 1.73	–2.80 ± 1.71	-3.55 ± 1.68	-2.20 ± 1.64
M15	b/1e-1	5.62 ± 0.05	5.78 ± 0.04	5.83 ± 0.05	5.59 ± 0.09	5.68 ± 0.04	5.61 ± 0.03	5.53 ± 0.03	5.50 ± 0.03	5.46 ± 0.03
M15	c/1e-2	–1.42 ± 0.04	–1.53 ± 0.03	–1.34 ± 0.04	–1.53 ± 0.03	–1.42 ± 0.03	–1.32 ± 0.03	–1.27 ± 0.03	–1.21 ± 0.03	–1.13 ± 0.03
M16	a/1e-4	9.81 ± 3.39	3.14 ± 3.06	0.38 ± 4.28	3.85 ± 3.48	6.30 ± 2.65	5.25 ± 2.13	2.32 ± 1.95	0.49 ± 1.90	1.14 ± 1.83
M16	b/1e-1	5.44 ± 0.06	5.52 ± 0.05	5.55 ± 0.07	5.47 ± 0.06	5.29 ± 0.04	5.28 ± 0.04	5.19 ± 0.03	5.17 ± 0.03	5.09 ± 0.03
M16	c/1e-2	–1.58 ± 0.04	–1.52 ± 0.03	–1.46 ± 0.03	–1.51 ± 0.03	–1.41 ± 0.02	–1.36 ± 0.02	–1.28 ± 0.02	–1.21 ± 0.02	–1.14 ± 0.02
M17	a/1e-4	-0.89 ± 3.92	-4.49 ± 3.39	–3.98 ± 3.71	–7.57 ± 4.51	–3.25 ± 2.74	–0.30 ± 2.47	–0.80 ± 2.36	–1.44 ± 2.17	–0.64 ± 2.08
M17	b/1e-1	5.81 ± 0.06	5.83 ± 0.06	5.85 ± 0.06	5.71 ± 0.07	5.65 ± 0.05	5.47 ± 0.04	5.48 ± 0.04	5.41 ± 0.04	5.28 ± 0.03
M17	c/1e-2	–1.54 ± 0.02	–1.52 ± 0.02	–1.41 ± 0.02	–1.25 ± 0.03	–1.33 ± 0.02	–1.22 ± 0.01	–1.21 ± 0.02	–1.16 ± 0.01	–1.08 ± 0.02
M18	a/1e-4	–1.88 ± 2.27	–5.55 ± 2.09	–5.94 ± 2.11	–1.53 ± 2.53	–2.21 ± 3.35	-0.75 ± 1.52	–1.19 ± 1.52	0.24 ± 1.51	0.93 ± 1.53
M18	b/1e-1	5.64 ± 0.04	5.68 ± 0.03	5.81 ± 0.03	5.60 ± 0.04	5.57 ± 0.05	5.46 ± 0.02	5.38 ± 0.02	5.38 ± 0.02	5.33 ± 0.02
M18	c/1e-2	–1.37 ± 0.02	–1.34 ± 0.02	–1.34 ± 0.02	–1.29 ± 0.02	–1.20 ± 0.02	–1.13 ± 0.02	–1.11 ± 0.02	–1.11 ± 0.02	–1.05 ± 0.02
M19	a/1e-4	11.82 ± 2.94	6.55 ± 2.78	5.01 ± 3.51	10.73 ± 3.34	9.32 ± 2.79	8.64 ± 2.51	10.22 ± 2.15	9.32 ± 2.21	11.03 ± 2.24
M19	b/1e-1	5.70 ± 0.05	5.88 ± 0.04	5.92 ± 0.06	5.67 ± 0.05	5.69 ± 0.04	5.61 ± 0.04	5.48 ± 0.03	5.43 ± 0.04	5.30 ± 0.04
M19	c/1e-2	–1.76 ± 0.03	–1.75 ± 0.03	–1.59 ± 0.03	–1.60 ± 0.04	–1.57 ± 0.03	–1.50 ± 0.03	–1.44 ± 0.03	–1.36 ± 0.03	–1.25 ± 0.03

Table 4 Details of Fitting Parameters of System Temperature for all 19 Beams

Beam	Paras	Freq (MHz)								
		1050	1100	1150	1200	1250	1300	1350	1400	1450
M01	P_0	4.94 ± 0.01	5.83 ± 0.01	4.36 ± 0.01	4.24 ± 0.03	4.35 ± 0.02	3.60 ± 0.01	3.10 ± 0.01	2.76 ± 0.01	2.00 ± 0.01
M01	P_1	9.12 ± 0.02	8.75 ± 0.03	7.53 ± 0.03	7.75 ± 0.08	6.88 ± 0.04	9.88 ± 0.03	10.03 ± 0.04	10.00 ± 0.04	11.93 ± 0.07
M01	P_2	26.31 ± 0.01	28.14 ± 0.01	26.89 ± 0.01	27.19 ± 0.02	25.54 ± 0.01	24.59 ± 0.01	23.91 ± 0.00	23.47 ± 0.00	22.23 ± 0.00
M01	n	1.37 ± 0.00	1.34 ± 0.00	1.26 ± 0.00	1.27 ± 0.01	1.21 ± 0.00	1.41 ± 0.00	1.43 ± 0.00	1.42 ± 0.00	1.53 ± 0.00
M02	P_0	4.10 ± 0.00	4.53 ± 0.01	4.23 ± 0.02	4.17 ± 0.05	4.08 ± 0.02	3.20 ± 0.00	2.47 ± 0.00	2.29 ± 0.00	1.49 ± 0.00
M02	P_1	7.68 ± 0.01	7.89 ± 0.03	6.19 ± 0.03	6.32 ± 0.07	5.73 ± 0.03	8.83 ± 0.02	9.36 ± 0.02	9.32 ± 0.02	11.41 ± 0.06
M02	P_2	25.65 ± 0.00	26.74 ± 0.01	26.63 ± 0.02	27.53 ± 0.04	25.56 ± 0.02	24.14 ± 0.00	23.29 ± 0.00	23.23 ± 0.00	21.87 ± 0.00
M02	n	1.25 ± 0.00	1.28 ± 0.00	1.10 ± 0.00	1.12 ± 0.01	1.07 ± 0.00	1.33 ± 0.00	1.37 ± 0.00	1.37 ± 0.00	1.48 ± 0.00
M03	P_0	4.89 ± 0.01	5.22 ± 0.01	4.92 ± 0.02	4.31 ± 0.02	4.70 ± 0.02	3.69 ± 0.01	3.10 ± 0.00	2.80 ± 0.01	2.01 ± 0.01
M03	P_1	8.16 ± 0.02	8.12 ± 0.03	6.53 ± 0.02	7.59 ± 0.06	6.29 ± 0.03	8.83 ± 0.03	9.46 ± 0.03	9.32 ± 0.04	10.91 ± 0.06
M03	P_2	27.87 ± 0.01	28.30 ± 0.01	27.66 ± 0.01	27.93 ± 0.02	26.41 ± 0.02	24.67 ± 0.01	23.34 ± 0.00	23.22 ± 0.01	21.86 ± 0.00
M03	n	1.29 ± 0.00	1.29 ± 0.00	1.15 ± 0.00	1.25 ± 0.01	1.12 ± 0.00	1.33 ± 0.00	1.39 ± 0.00	1.37 ± 0.00	1.46 ± 0.00
M04	P_0	4.23 ± 0.00	5.00 ± 0.01	3.52 ± 0.01	3.24 ± 0.02	3.60 ± 0.01	2.70 ± 0.00	2.42 ± 0.00	2.08 ± 0.00	1.31 ± 0.00
M04	P_1	8.05 ± 0.01	8.10 ± 0.03	7.31 ± 0.03	7.31 ± 0.08	6.20 ± 0.03	8.88 ± 0.02	9.47 ± 0.02	9.35 ± 0.02	12.18 ± 0.05
M04	P_2	26.10 ± 0.00	27.88 ± 0.01	26.48 ± 0.01	27.47 ± 0.02	26.43 ± 0.01	25.13 ± 0.00	24.59 ± 0.00	23.92 ± 0.00	22.13 ± 0.00
M04	n	1.30 ± 0.00	1.31 ± 0.00	1.26 ± 0.00	1.25 ± 0.01	1.15 ± 0.00	1.36 ± 0.00	1.40 ± 0.00	1.40 ± 0.00	1.56 ± 0.00
M05	P_0	4.38 ± 0.00	4.75 ± 0.01	3.43 ± 0.01	3.19 ± 0.03	3.50 ± 0.01	2.82 ± 0.00	2.47 ± 0.00	2.09 ± 0.00	1.41 ± 0.00
M05	P_1	8.18 ± 0.01	8.44 ± 0.03	6.79 ± 0.03	6.69 ± 0.09	6.42 ± 0.04	8.59 ± 0.02	9.29 ± 0.02	9.49 ± 0.02	11.49 ± 0.05
M05	P_2	26.13 ± 0.00	27.32 ± 0.01	26.06 ± 0.01	26.75 ± 0.02	25.96 ± 0.01	24.51 ± 0.00	23.88 ± 0.00	23.76 ± 0.00	22.65 ± 0.00
M05	n	1.32 ± 0.00	1.34 ± 0.00	1.21 ± 0.00	1.20 ± 0.01	1.19 ± 0.00	1.34 ± 0.00	1.40 ± 0.00	1.41 ± 0.00	1.52 ± 0.00
M06	P_0	5.28 ± 0.01	6.22 ± 0.02	4.54 ± 0.02	4.29 ± 0.03	4.65 ± 0.02	3.77 ± 0.01	3.28 ± 0.01	2.99 ± 0.01	2.23 ± 0.01
M06	P_1	9.01 ± 0.03	8.49 ± 0.04	7.29 ± 0.05	7.96 ± 0.08	7.25 ± 0.04	9.39 ± 0.04	10.41 ± 0.05	10.16 ± 0.06	11.65 ± 0.09
M06	P_2	27.57 ± 0.01	29.40 ± 0.02	27.50 ± 0.02	28.62 ± 0.03	26.86 ± 0.02	25.10 ± 0.01	24.27 ± 0.01	23.75 ± 0.01	22.46 ± 0.01
M06	n	1.35 ± 0.00	1.32 ± 0.00	1.23 ± 0.00	1.27 ± 0.01	1.22 ± 0.00	1.37 ± 0.00	1.45 ± 0.00	1.42 ± 0.00	1.50 ± 0.00
M07	P_0	3.72 ± 0.00	4.43 ± 0.02	3.44 ± 0.02	3.34 ± 0.03	3.38 ± 0.01	2.88 ± 0.00	2.24 ± 0.00	1.95 ± 0.00	1.25 ± 0.00
M07	P_1	8.78 ± 0.02	8.15 ± 0.05	6.38 ± 0.04	6.94 ± 0.08	6.41 ± 0.03	9.30 ± 0.02	10.59 ± 0.03	10.72 ± 0.04	13.50 ± 0.10
M07	P_2	26.36 ± 0.00	27.90 ± 0.01	26.27 ± 0.01	27.01 ± 0.03	25.08 ± 0.01	24.22 ± 0.00	23.02 ± 0.00	22.70 ± 0.00	21.36 ± 0.00
M07	n	1.35 ± 0.00	1.30 ± 0.00	1.16 ± 0.00	1.19 ± 0.01	1.16 ± 0.00	1.38 ± 0.00	1.46 ± 0.00	1.47 ± 0.00	1.61 ± 0.00
M08	P_0	4.57 ± 0.01	3.93 ± 0.01	4.85 ± 0.04	4.33 ± 0.04	3.96 ± 0.02	3.20 ± 0.01	2.63 ± 0.01	2.24 ± 0.01	1.77 ± 0.01
M08	P_1	7.17 ± 0.02	7.87 ± 0.03	5.78 ± 0.02	6.80 ± 0.06	6.40 ± 0.03	8.69 ± 0.03	9.06 ± 0.05	9.87 ± 0.06	11.21 ± 0.09
M08	P_2	25.78 ± 0.01	25.29 ± 0.01	27.01 ± 0.04	27.23 ± 0.04	24.97 ± 0.02	23.97 ± 0.01	22.68 ± 0.01	22.43 ± 0.01	21.43 ± 0.01
M08	n	1.17 ± 0.00	1.25 ± 0.00	1.02 ± 0.00	1.14 ± 0.01	1.10 ± 0.00	1.30 ± 0.00	1.34 ± 0.00	1.38 ± 0.00	1.46 ± 0.00
M09	P_0	3.47 ± 0.01	3.53 ± 0.01	3.28 ± 0.02	3.28 ± 0.02	3.18 ± 0.02	2.61 ± 0.01	2.07 ± 0.01	1.72 ± 0.00	1.26 ± 0.00
M09	P_1	8.88 ± 0.02	9.07 ± 0.05	7.01 ± 0.05	8.56 ± 0.10	7.15 ± 0.06	11.58 ± 0.07	12.20 ± 0.09	13.30 ± 0.11	17.47 ± 0.22
M09	P_2	25.34 ± 0.00	25.91 ± 0.01	25.78 ± 0.01	26.73 ± 0.02	25.03 ± 0.02	24.10 ± 0.01	23.22 ± 0.01	22.99 ± 0.00	21.81 ± 0.00
M09	n	1.34 ± 0.00	1.36 ± 0.00	1.20 ± 0.00	1.33 ± 0.01	1.22 ± 0.01	1.51 ± 0.00	1.55 ± 0.00	1.60 ± 0.01	1.76 ± 0.01
M10	P_0	3.96 ± 0.00	3.79 ± 0.01	3.68 ± 0.01	3.49 ± 0.02	3.42 ± 0.01	2.80 ± 0.00	2.33 ± 0.00	1.93 ± 0.00	1.41 ± 0.00
M10	P_1	6.83 ± 0.01	7.30 ± 0.01	5.43 ± 0.01	6.64 ± 0.04	5.78 ± 0.02	7.75 ± 0.01	8.41 ± 0.02	8.59 ± 0.02	10.30 ± 0.03
M10	P_2	25.98 ± 0.00	26.39 ± 0.00	26.23 ± 0.01	26.51 ± 0.01	24.95 ± 0.01	23.77 ± 0.00	23.21 ± 0.00	22.64 ± 0.00	21.54 ± 0.00
M10	n	1.18 ± 0.00	1.22 ± 0.00	1.04 ± 0.00	1.16 ± 0.00	1.08 ± 0.00	1.25 ± 0.00	1.30 ± 0.00	1.32 ± 0.00	1.43 ± 0.00
M11	P_0	4.91 ± 0.01	5.14 ± 0.01	4.41 ± 0.01	4.03 ± 0.02	4.02 ± 0.01	3.39 ± 0.01	3.02 ± 0.01	2.70 ± 0.01	1.95 ± 0.01
M11	P_1	8.77 ± 0.03	8.48 ± 0.04	7.85 ± 0.03	9.20 ± 0.08	7.58 ± 0.03	9.63 ± 0.04	10.56 ± 0.05	10.49 ± 0.05	12.10 ± 0.08
M11	P_2	27.18 ± 0.01	28.28 ± 0.01	27.61 ± 0.01	27.91 ± 0.02	25.57 ± 0.01	24.46 ± 0.01	24.18 ± 0.01	24.07 ± 0.01	23.14 ± 0.00
M11	n	1.33 ± 0.00	1.31 ± 0.00	1.26 ± 0.00	1.35 ± 0.01	1.24 ± 0.00	1.38 ± 0.00	1.45 ± 0.00	1.44 ± 0.00	1.52 ± 0.00
M12	P_0	4.74 ± 0.01	4.62 ± 0.01	3.94 ± 0.01	3.51 ± 0.02	3.44 ± 0.01	2.90 ± 0.01	2.65 ± 0.00	2.35 ± 0.01	1.66 ± 0.01
M12	P_1	7.44 ± 0.02	7.82 ± 0.02	7.00 ± 0.02	8.36 ± 0.09	6.68 ± 0.03	8.30 ± 0.03	8.85 ± 0.03	8.39 ± 0.03	9.72 ± 0.06
M12	P_2	28.58 ± 0.01	28.71 ± 0.01	28.31 ± 0.01	28.76 ± 0.02	25.83 ± 0.01	24.49 ± 0.01	24.16 ± 0.00	23.77 ± 0.00	22.47 ± 0.00
M12	n	1.24 ± 0.00	1.28 ± 0.00	1.20 ± 0.00	1.30 ± 0.01	1.18 ± 0.00	1.30 ± 0.00	1.35 ± 0.00	1.31 ± 0.00	1.39 ± 0.00
M13	P_0	5.46 ± 0.01	6.30 ± 0.02	4.78 ± 0.02	4.27 ± 0.02	4.31 ± 0.02	3.69 ± 0.01	3.38 ± 0.01	3.14 ± 0.01	2.33 ± 0.01
M13	P_1	8.62 ± 0.04	7.76 ± 0.04	7.53 ± 0.03	8.90 ± 0.08	7.41 ± 0.04	9.08 ± 0.05	8.92 ± 0.05	9.00 ± 0.05	10.57 ± 0.08
M13	P_2	27.97 ± 0.01	29.57 ± 0.02	28.34 ± 0.01	28.26 ± 0.02	25.94 ± 0.02	24.82 ± 0.01	24.14 ± 0.01	23.82 ± 0.01	22.29 ± 0.01
M13	n	1.32 ± 0.00	1.26 ± 0.00	1.23 ± 0.00	1.34 ± 0.01	1.23 ± 0.00	1.34 ± 0.00	1.34 ± 0.00	1.34 ± 0.00	1.44 ± 0.01
M14	P_0	4.76 ± 0.01	5.18 ± 0.02	4.32 ± 0.03	3.33 ± 0.03	3.68 ± 0.02	2.92 ± 0.01	2.56 ± 0.01	2.39 ± 0.01	1.73 ± 0.01
M14	P_1	8.69 ± 0.03	8.11 ± 0.04	7.10 ± 0.05	9.13 ± 0.11	7.40 ± 0.05	9.65 ± 0.06	10.67 ± 0.08	10.62 ± 0.08	13.43 ± 0.18
M14	P_2	28.24 ± 0.01	29.19 ± 0.02	27.85 ± 0.02	27.87 ± 0.02	27.31 ± 0.02	25.67 ± 0.01	24.39 ± 0.01	23.82 ± 0.01	22.24 ± 0.01
M14	n	1.32 ± 0.00	1.27 ± 0.00	1.19 ± 0.00	1.34 ± 0.01	1.20 ± 0.00	1.35 ± 0.00	1.44 ± 0.00	1.42 ± 0.00	1.55 ± 0.01

Table 4 *Continued.*

Beam	Paras	Freq (MHz)								
		1050	1100	1150	1200	1250	1300	1350	1400	1450
M15	P_0	4.13 ± 0.00	4.73 ± 0.01	4.33 ± 0.01	3.48 ± 0.02	3.26 ± 0.01	2.56 ± 0.00	2.32 ± 0.00	2.15 ± 0.00	1.39 ± 0.00
M15	P_1	8.49 ± 0.02	7.52 ± 0.02	5.52 ± 0.02	6.02 ± 0.04	6.46 ± 0.03	7.99 ± 0.02	7.92 ± 0.02	8.02 ± 0.02	11.21 ± 0.03
M15	P_2	25.79 ± 0.00	27.53 ± 0.01	27.69 ± 0.01	27.34 ± 0.02	24.98 ± 0.01	23.72 ± 0.00	23.08 ± 0.00	22.96 ± 0.00	21.65 ± 0.00
M15	n	1.35 ± 0.00	1.27 ± 0.00	1.09 ± 0.00	1.12 ± 0.00	1.20 ± 0.00	1.29 ± 0.00	1.29 ± 0.00	1.30 ± 0.00	1.51 ± 0.00
M16	P_0	6.83 ± 0.03	7.12 ± 0.03	6.59 ± 0.03	5.73 ± 0.05	5.65 ± 0.03	4.64 ± 0.02	4.17 ± 0.02	4.00 ± 0.02	3.23 ± 0.02
M16	P_1	8.69 ± 0.05	8.50 ± 0.05	7.54 ± 0.04	8.36 ± 0.08	7.57 ± 0.05	9.72 ± 0.07	9.71 ± 0.08	9.69 ± 0.08	10.65 ± 0.11
M16	P_2	29.72 ± 0.03	30.43 ± 0.03	29.61 ± 0.03	29.14 ± 0.05	27.19 ± 0.03	25.36 ± 0.02	24.23 ± 0.02	24.15 ± 0.02	23.00 ± 0.02
M16	n	1.30 ± 0.00	1.29 ± 0.00	1.21 ± 0.00	1.26 ± 0.01	1.20 ± 0.00	1.35 ± 0.00	1.36 ± 0.01	1.35 ± 0.01	1.40 ± 0.01
M17	P_0	4.67 ± 0.01	4.73 ± 0.01	4.10 ± 0.02	3.44 ± 0.03	3.90 ± 0.02	3.27 ± 0.01	2.67 ± 0.01	2.39 ± 0.00	1.74 ± 0.01
M17	P_1	7.77 ± 0.02	7.62 ± 0.03	5.93 ± 0.03	6.74 ± 0.07	6.02 ± 0.03	8.20 ± 0.02	8.84 ± 0.04	8.68 ± 0.03	9.45 ± 0.05
M17	P_2	27.07 ± 0.01	27.82 ± 0.01	26.74 ± 0.02	27.70 ± 0.03	26.60 ± 0.02	25.23 ± 0.01	23.98 ± 0.01	23.48 ± 0.00	22.20 ± 0.01
M17	n	1.26 ± 0.00	1.25 ± 0.00	1.10 ± 0.00	1.15 ± 0.01	1.10 ± 0.00	1.27 ± 0.00	1.33 ± 0.00	1.32 ± 0.00	1.36 ± 0.00
M18	P_0	5.58 ± 0.01	5.76 ± 0.02	5.85 ± 0.05	4.83 ± 0.04	5.35 ± 0.03	4.28 ± 0.01	3.78 ± 0.01	3.31 ± 0.01	2.66 ± 0.01
M18	P_1	7.37 ± 0.02	7.36 ± 0.02	5.66 ± 0.03	7.19 ± 0.06	6.14 ± 0.02	7.95 ± 0.02	8.05 ± 0.03	8.52 ± 0.03	9.23 ± 0.04
M18	P_2	28.15 ± 0.01	29.09 ± 0.02	29.67 ± 0.06	29.79 ± 0.04	27.99 ± 0.03	25.97 ± 0.01	24.88 ± 0.01	24.46 ± 0.01	23.24 ± 0.01
M18	n	1.19 ± 0.00	1.19 ± 0.00	1.01 ± 0.00	1.18 ± 0.01	1.07 ± 0.00	1.24 ± 0.00	1.23 ± 0.00	1.27 ± 0.00	1.31 ± 0.00
M19	P_0	4.56 ± 0.02	4.36 ± 0.02	4.70 ± 0.03	4.10 ± 0.03	4.13 ± 0.02	3.38 ± 0.01	2.82 ± 0.01	2.52 ± 0.01	1.96 ± 0.01
M19	P_1	8.61 ± 0.06	9.10 ± 0.05	7.01 ± 0.04	8.58 ± 0.09	7.50 ± 0.04	11.19 ± 0.07	11.27 ± 0.09	11.59 ± 0.11	13.00 ± 0.18
M19	P_2	27.90 ± 0.02	27.57 ± 0.02	28.21 ± 0.03	28.10 ± 0.03	25.91 ± 0.02	24.49 ± 0.01	23.51 ± 0.01	23.29 ± 0.01	21.95 ± 0.01
M19	n	1.29 ± 0.00	1.32 ± 0.00	1.14 ± 0.00	1.28 ± 0.01	1.19 ± 0.00	1.44 ± 0.00	1.44 ± 0.01	1.46 ± 0.01	1.53 ± 0.01

Table 5 The gain information for 19 beams within ZA of 26.4°. The mean value of gain for Beam 1 is expressed in the unit of K Jy^{-1}. For the other 18 beams, the ratio compared to the gain value of beam 1 at the same frequency is presented.

Beam	Gain (K Jy^{-1}) / Ratio								
	1050	1100	1150	1200	1250	1300	1350	1400	1450
M01	15.98 ± 0.27	16.27 ± 0.21	16.48 ± 0.14	16.10 ± 0.25	16.12 ± 0.25	15.94 ± 0.28	15.98 ± 0.27	16.02 ± 0.26	15.71 ± 0.29
M02	0.98 ± 0.03	0.95 ± 0.03	0.95 ± 0.03	0.95 ± 0.03	0.95 ± 0.03	0.93 ± 0.03	0.94 ± 0.02	0.94 ± 0.02	0.95 ± 0.03
M03	1.03 ± 0.03	0.99 ± 0.03	1.00 ± 0.03	1.00 ± 0.04	1.00 ± 0.03	0.99 ± 0.03	0.97 ± 0.03	0.97 ± 0.03	0.98 ± 0.03
M04	1.01 ± 0.04	0.97 ± 0.03	0.98 ± 0.03	0.97 ± 0.04	0.97 ± 0.04	0.96 ± 0.03	0.95 ± 0.03	0.95 ± 0.03	0.95 ± 0.03
M05	1.02 ± 0.03	1.01 ± 0.02	1.03 ± 0.02	1.00 ± 0.03	1.00 ± 0.03	0.99 ± 0.02	0.97 ± 0.02	0.98 ± 0.02	0.98 ± 0.03
M06	0.99 ± 0.03	0.98 ± 0.02	0.98 ± 0.03	0.96 ± 0.04	0.96 ± 0.03	0.95 ± 0.02	0.94 ± 0.02	0.94 ± 0.02	0.94 ± 0.02
M07	0.98 ± 0.02	0.95 ± 0.02	0.96 ± 0.02	0.94 ± 0.03	0.96 ± 0.03	0.95 ± 0.02	0.94 ± 0.02	0.93 ± 0.02	0.93 ± 0.02
M08	0.96 ± 0.03	0.94 ± 0.03	0.93 ± 0.03	0.93 ± 0.04	0.92 ± 0.03	0.92 ± 0.03	0.91 ± 0.03	0.89 ± 0.03	0.89 ± 0.03
M09	0.95 ± 0.02	0.94 ± 0.02	0.92 ± 0.02	0.91 ± 0.02	0.92 ± 0.02	0.93 ± 0.02	0.91 ± 0.02	0.89 ± 0.02	0.90 ± 0.02
M10	0.99 ± 0.03	0.97 ± 0.03	0.97 ± 0.03	0.96 ± 0.04	0.97 ± 0.03	0.96 ± 0.03	0.96 ± 0.03	0.95 ± 0.03	0.95 ± 0.03
M11	0.96 ± 0.04	0.94 ± 0.04	0.94 ± 0.03	0.93 ± 0.05	0.93 ± 0.04	0.92 ± 0.03	0.92 ± 0.03	0.91 ± 0.03	0.91 ± 0.03
M12	0.96 ± 0.05	0.93 ± 0.04	0.92 ± 0.03	0.94 ± 0.04	0.94 ± 0.03	0.91 ± 0.03	0.90 ± 0.03	0.89 ± 0.02	0.90 ± 0.03
M13	0.99 ± 0.04	0.96 ± 0.03	0.97 ± 0.03	0.99 ± 0.04	0.96 ± 0.03	0.97 ± 0.03	0.96 ± 0.03	0.95 ± 0.03	0.95 ± 0.03
M14	0.95 ± 0.03	0.94 ± 0.03	0.93 ± 0.03	0.92 ± 0.04	0.93 ± 0.04	0.93 ± 0.03	0.92 ± 0.02	0.91 ± 0.02	0.91 ± 0.02
M15	0.90 ± 0.03	0.91 ± 0.02	0.90 ± 0.02	0.90 ± 0.05	0.90 ± 0.02	0.90 ± 0.02	0.88 ± 0.02	0.87 ± 0.02	0.88 ± 0.02
M16	0.90 ± 0.03	0.88 ± 0.02	0.86 ± 0.03	0.88 ± 0.03	0.86 ± 0.02	0.86 ± 0.02	0.84 ± 0.02	0.83 ± 0.02	0.83 ± 0.02
M17	0.93 ± 0.03	0.91 ± 0.03	0.90 ± 0.03	0.89 ± 0.04	0.89 ± 0.02	0.88 ± 0.02	0.88 ± 0.02	0.86 ± 0.02	0.86 ± 0.02
M18	0.90 ± 0.02	0.88 ± 0.02	0.89 ± 0.02	0.89 ± 0.02	0.88 ± 0.03	0.87 ± 0.02	0.86 ± 0.02	0.86 ± 0.02	0.87 ± 0.02
M19	0.94 ± 0.03	0.94 ± 0.02	0.93 ± 0.03	0.93 ± 0.03	0.93 ± 0.03	0.92 ± 0.03	0.90 ± 0.02	0.89 ± 0.02	0.89 ± 0.03

3 BACKEND

3.1 Stability and Sensitivity of Spectral Baseline

Stability and sensitivity are two fundamental properties associated with spectral baseline. Stability represents fluctuation level of a baseline in a time range. Sensitivity represents response capability of a spectrometer. We estimated stability and sensitivity by taking observations toward the HI galaxy NGC 672 in 2019 April 20.

A set of 30 min observations without injection of noise signal was taken to test stability of the baseline. Averaged bandpass spectra per 5 min are displayed in Figure 13. The variation of bandpass is ∼4% in 30 min.

In order to measure sensitivity performance of the backend, noise signal as described in Section 2.1 was injected to calibrate observed spectra. Both noise signals with high and low intensity were injected for 5 min. The unit of the spectrum was then calibrated into kelvin through

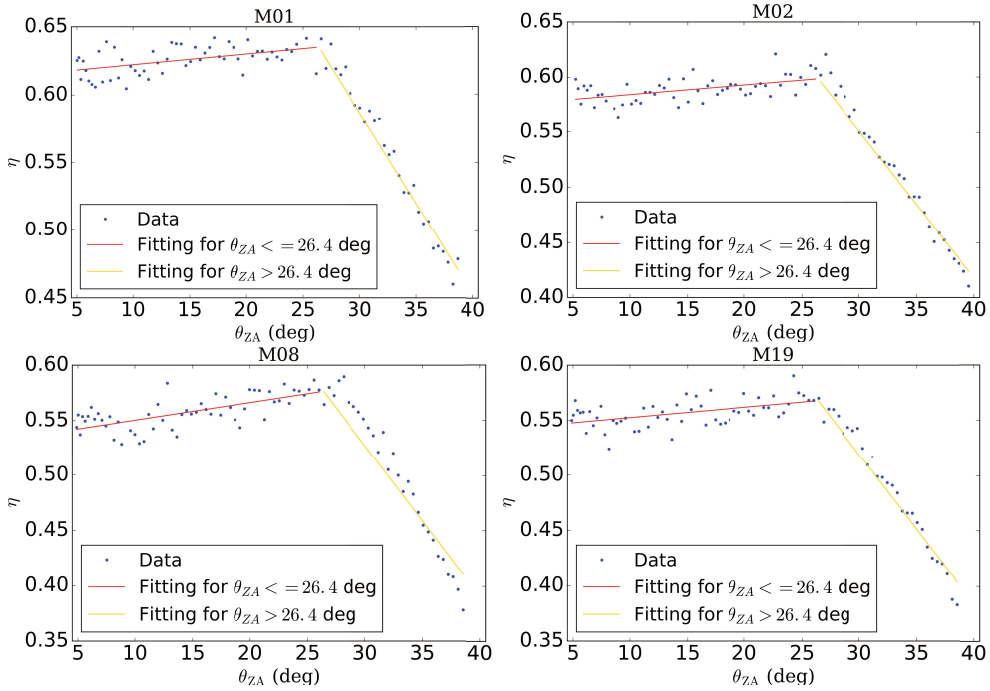

Fig. 11 Measured η curve as a function of ZA $\theta_{\rm ZA}$ at 1400 MHz for Beams 1, 2, 8 and 19. Fitting results when $\theta_{\rm ZA} \leq 26.4^{\circ}$ and $\theta_{\rm ZA} > 26.4^{\circ}$ are represented with red and gold solid lines, respectively.

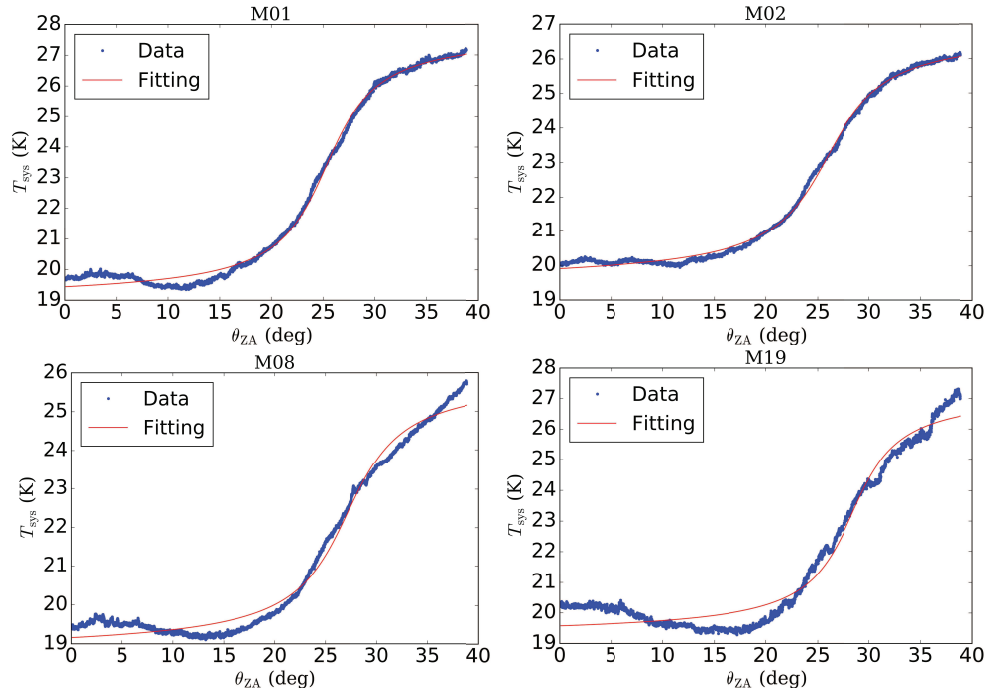

Fig. 12 Measured $T_{\rm sys}$ curve as a function of ZA $\theta_{\rm ZA}$ at 1400 MHz for Beams 1, 2, 8 and 19. The fitting result is represented with a red solid line.

the following transformation,

$$T_A = T_{\rm cal} \frac{P_{\rm off}^{\rm cal}}{P_{\rm on}^{\rm cal} - P_{\rm off}^{\rm cal}}, \quad (8)$$

where $T_{\rm A}$ is calibrated antenna temperature. $T_{\rm cal}$ is noise diode temperature as shown in Figure 1 and Figure 2. $P_{\rm on}$ and $P_{\rm off}$ are power values when noise diode is on and off, respectively. As demonstrated in Figure 14, the derived continuum levels under high and low noise injection are consistent within 1%.

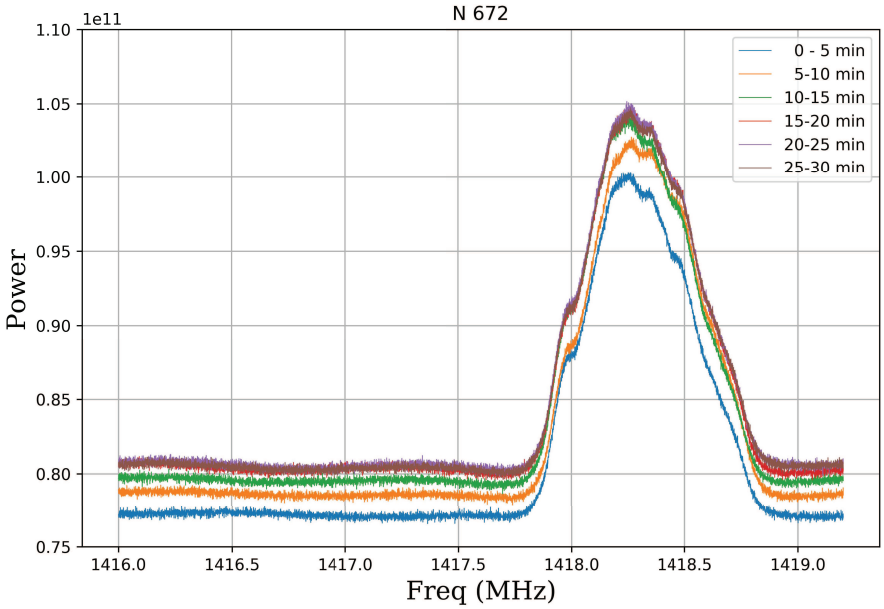

Fig. 13 Variance of spectral baseline toward NGC 672 in 30 min. Each spectrum is averaged in a time bin of 5 min.

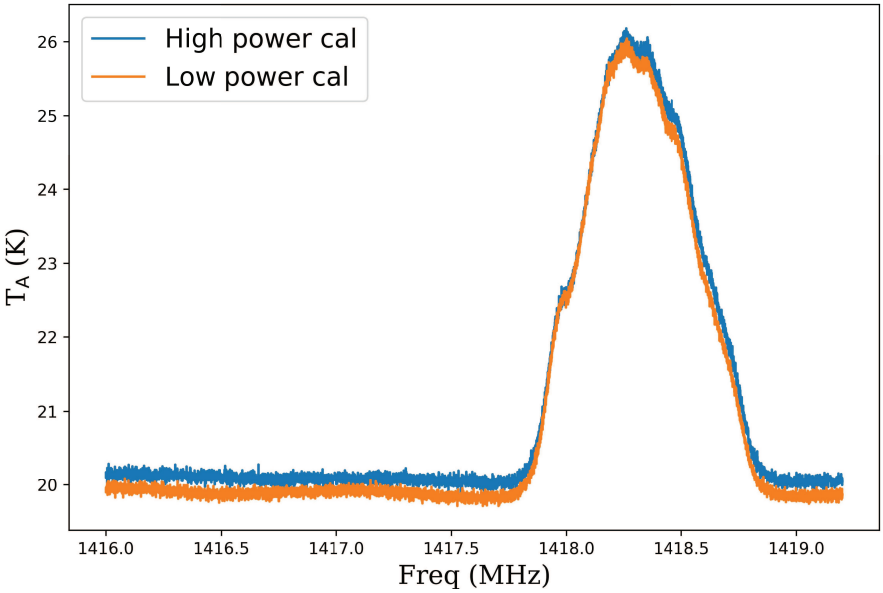

Fig. 14 Calibrated HI spectrum under high power cal (*blue*) and low power cal (*orange*).

We estimated sensitivity with RMS of a spectrum. RMS is calculated with line-free frequency range. For the total ON mode, the expected RMS of an averaged spectrum of two polarizations $\sigma_{\rm T}$ is connected with system temperature $T_{\rm sys}$, channel resolution β and integration time τ with $\sigma_T = T_{\rm sys}/\sqrt{2\beta\tau}$. Periodic injection of high and low noise would lead to increase of $T_{\rm sys}$ by 5.4 K and 0.5 K during an observation cycle (half time for cal ON and half time for cal OFF), respectively. Comparison between obtained and theoretical RMS is demonstrated in Table 6. It is obvious that performance of the 19 beam backend is very consistent with that of theoretical value for both low and high intensity noise injection.

3.2 Standing Waves

The antenna structure and radio frequency (RF) devices of a radio telescope can cause reflection of electromagnetic (EM) waves. The coherent superposition of the received signal and its reflected wave results in periodic fluctuations in the frequency bandpass, which is called a “standing wave.” This is a common phenomenon seen in spec-

troscopic observations with radio telescopes (i.e., Briggs et al. 1997; Popping & Braun 2008). The major contribution to the standing wave for FAST is caused by reflection between the dish and receiver cabin. The relation between the standing wave frequency and reflecting distance is given by Equation (9)

$$D = \frac{c}{2\,\Delta f}, \tag{9}$$

where D is the distance between the receiver cabin and the dish, c is the speed of light and Δf is the width of the frequency ripple. The value of D is $\sim$ 138 m for FAST, leading to $\Delta f \sim 1$ MHz. At L-band, the corresponding velocity width of Δf is $\sim 200\,\mathrm{km\,s^{-1}}$, which is located within the range of interest for extragalactic HI observations.

Efforts have been put into analyzing and minimizing the standing wave effects of FAST. To identify the major contribution to the FAST standing wave, we checked the bandpass when the receiver cabin was rising. The width of the frequency ripple varies with the cabin height following the relation defined by Equation 9. This experiment was done with the cabin dock uncovered. Thus the ground radiation passing through the central hole of the dish serves as the EM source for the standing wave. In Figure 15, the plots in the upper panels display the bandpass before the cabin dock is covered with metal mesh and those from the lower panel are after. The fluctuation declines significantly when ground radiation is blocked out.

Feed leakage emission can be another EM source for the standing wave, since the horns emit an EM wave when the calibration noise diode is fired up. Figure 15 exhibits the bandpasses with high power noise diode (left column plots) and with low power noise diode (right column plots). It can be seen that the signal from the high power noise diode ($\sim$ 10 K) affects the bandpass fluctuation, whereas the low power signal ($\sim$ 1 K) does not.

The standing wave at different ZAs has also been checked and yet no significant difference was found. Figure 16 features a comparison of the spectra bandpass from ZA = 2.7°and 36.7°. The data are fitted to a sine function. The major fitting parameters are amplitude, phase and period. The relative differences of those parameters are 12.4%, 10.7% and 0.6% respectively. Stable ripple patterns are expected since the distance between the receiver cabin and the apex of the parabolic dish should remain unchanged during observing.

The bandpass difference is smaller when the ZA difference is smaller, so the ON/OFF position switch technique can be used to calibrate the baseline and to decrease the standing wave ripples. Figure 17 shows the standing wave test from the ON/OFF observation towards J073631.82+383058.3. The top and middle panels are the calibrated bandpasses from the ON- and OFF- positions respectively. The bottom panel is the ON-OFF calibrated bandpass and a sine function fitting result, which manifests a ripple amplitude of $\sim$ 15 mK.

Other testing observations were obtained toward NGC 2718 under ON-OFF mode. As exhibited in Figure 18, the amplitude of the standing wave varies with frequency.

Table 6 RMS value of 5 min observations toward NGC 672. Channel resolution is 0.476 kHz during calculation.

Cal Intensity	Obtained value (mK)	Theoretical value (mK)
Low	40.1	38.4
High	48.0	47.7

3.3 Polarization

We carried out FAST polarization observations of 3C 286 to measure the instrumental polarization of the telescope in Oct. 2018. 3C 286 is a standard polarization calibrator with stable polarization degrees and polarization angles from 1 to 50 GHz (Perley & Butler 2013). 3C 286 was drifted at parallactic angles of –60, –30, 0, 30 and 60 degrees through the central beam of the 19-beam receiver. The strength of the noise diode was set to 1 K with on-off period of 0.2 s. The four correlations of the XX, YY, XY and YX signals were simultaneously recorded with ROACH backends in both the spectral line modes of 500 MHz bandwidth and 32 MHz bandwidth. The data reduction including the gain and phase calibration of the system, the calibration of the four correlated spectra and the derivation of the instrumental polarization using the data at five parallactic angles was carried out with the RHSTK package. Figure 19 shows the measurements of the Stokes Q, U and V parameters of 3C 286 at five parallactic angles. By fitting the sinusoidal behaviors of the Stokes parameters as functions of parallactic angles, the polarization degree and polarization angle of 3C 286 are 6.6% +/- 1.5 % and 33.4 +/- 6.4 degrees, respectively. Our calibrated polarization results of 3C 286 are close to the values of 9.47% +/- 0.02 % and 33 +/- 1 degrees in Perley & Butler (2013). The instrumental polarization parameters of FAST obtained from the data were close to being unitary, indicating a good isolation between the two signal paths of linear polarization feeds and a good performance of the polarization facility of FAST. We expect that with better characterization of the polarization prop-

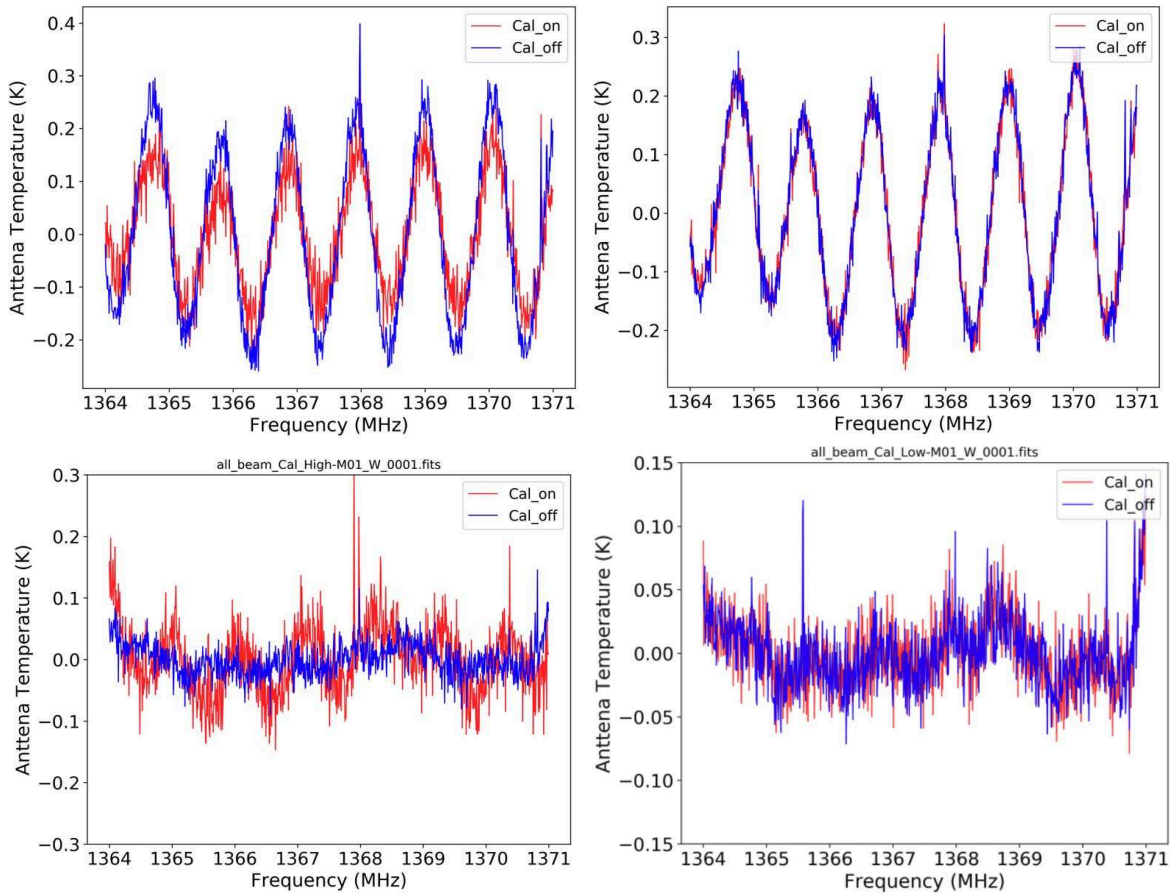

Fig. 15 A comparison of the bandpass ripples before (*upper panels*) and after (*lower panels*) the cabin dock platform is covered with metal mesh. The *left* panels feature high power noise diode injection and the *right* panels demonstrate low noise power.

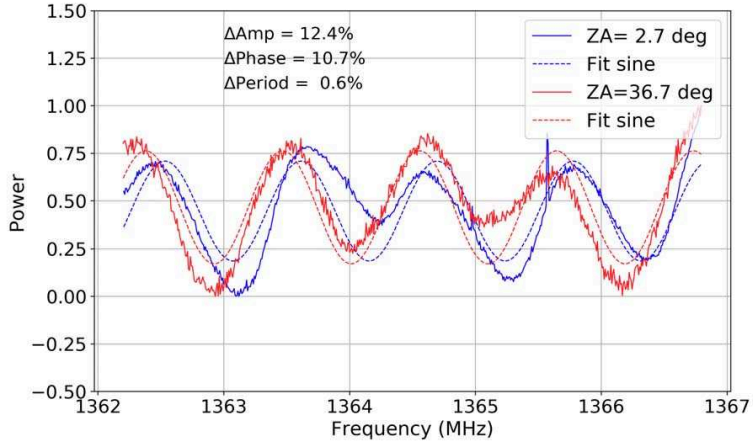

Fig. 16 Bandpass ripples at different ZAs. The blue line is the spectrum obtained with drift-scan observation at ZA = 2.7° and the red line is that at ZA = 36.7°. The dashed lines are the sine function fitting results. A linear baseline removal was processed beforehand. The intensity of the spectra is normalized and the unit is relative power.

erties including the pointing accuracy, beam width, beam squint and beam squash of FAST, the polarization data will be calibrated to an accuracy of 0.1%–0.01 %, in order to carry out scientific spectral line polarization observations in the near future.

4 OBSERVATION

4.1 Observation Modes

Now there are eight observation modes in FAST. The details are listed in the following.

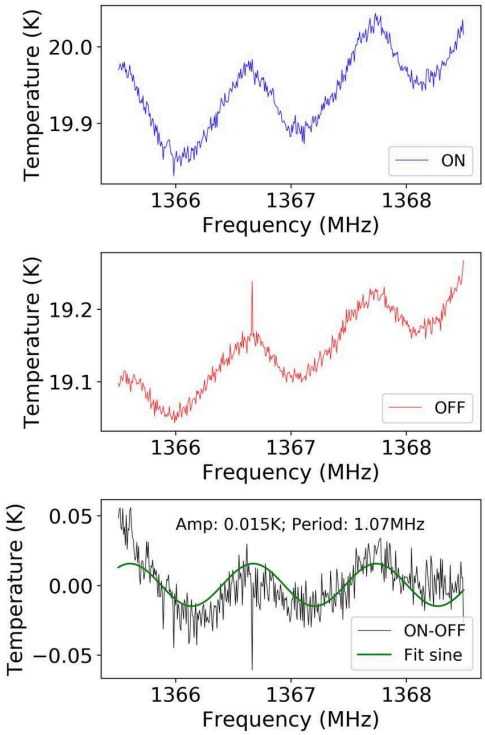

Fig. 17 Standing wave test from the ON/OFF observation towards J073631.82+383058.3. The top and middle panels are the calibrated bandpasses from ON- and OFF-positions. The bottom panel is the ON-OFF calibrated bandpass with a linear baseline removed. The sine function is fit to the spectrum, which gives the amplitude of the standing wave ~ 15 mK.

1. Drifting scan. In this mode, the position of the feed cabin is fixed. To avoid pointing offset by the cooling of oil in the actuator, the actuators employed for shaping the paraboloid surface are adjusted continually to keep the same paraboloidal shape in this mode. The telescope points across the sky as the Earth rotates. There are four parameters in this mode, source name, source coordinate in J2000 system, observational time range and rotation angle that represents the cross angle between the line along beams 8, 2, 1, 5 and 14 and line of Dec. The rotation angle has a limit of [–80,80] degree.
2. Total power. In this mode, the source can be tracked continuously. Tracking time for a source at different latitude is plotted in Figure 20. Three parameters including source name, coordinate and integration time are needed. Derived RMS of the averaged spectrum for both polarizations is estimated with,

$$\sigma = \frac{T_{\rm sys}}{\sqrt{2\beta\tau}}\ {\rm K}, \tag{10}$$

   where β=1.2$\rm B_{chan}$. $\rm B_{chan}$ is channel width of the spectrometer in the unit of Hz.
3. Position switch. The design of position mode is to achieve quick switch between source ON and source OFF in order to reduce baseline variation. There are five parameters in this mode.
   – Coordinate of ON position.
   – Coordinate of OFF position. The position of OFF source is designed to be within 1 degree from that of ON source.
   – Integration time of ON source.
   – Integration time of OFF source.
   – Times of ON-OFF cycle.

   Overhead time between ON and OFF position depends on separation of ON and OFF position, $\Delta\theta$. It is 30 s for $\Delta\theta < 20'$ and is 60 s for $20' \leq \Delta\theta < 60'$.
   Derived RMS of each spectrum with both polarizations is estimated with,

$$\sigma = \frac{T_{\rm sys}}{\sqrt{\beta\tau}}\ {\rm K}\,, \tag{11}$$

   where β=1.2$\rm B_{chan}$. $\rm B_{chan}$ is channel width of the spectrometer in the unit of Hz.
4. On-the-fly (OTF) mapping. This mode is designed for mapping a sky area with Beam 1 only. Six parameters are necessary for observation: source name, source position, observational time range, sky coverage (e.g., $7'\times7'$ of the mapping region), scanning separation (e.g., $1'$) between two parallel scanning lines and s-

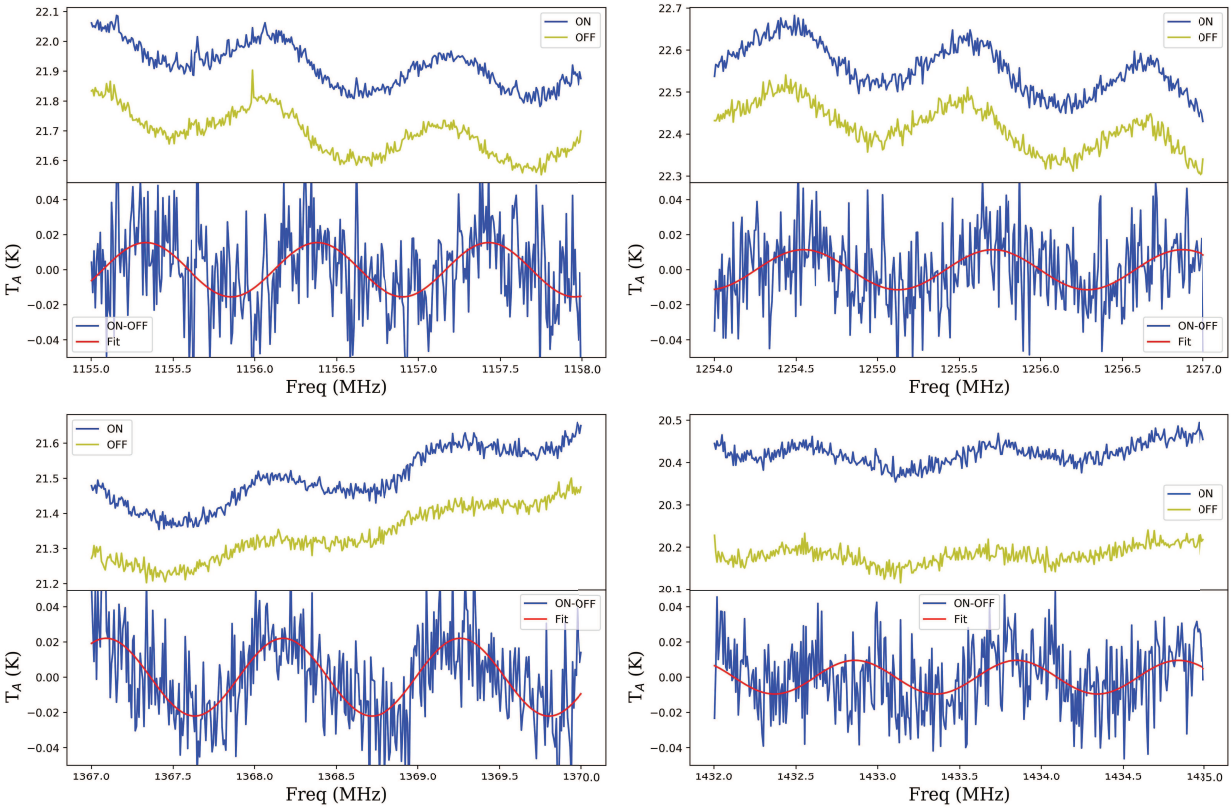

Fig. 18 Bandpass spectrum at different frequency ranges during ON-OFF observations towards NGC 2718. The amplitudes of the standing wave in frequency ranges of [1150,1158], [1254,1257], [1367,1370] and [1432,1435] MHz are 15, 11, 22 and 9.5 mK, respectively.

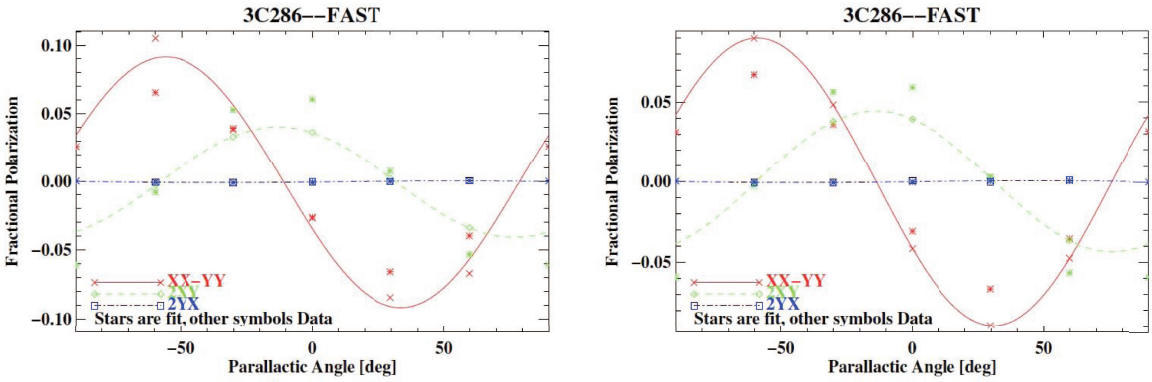

Fig. 19 The measurements and fits for the Stokes Q, U and V parameters of 3C 286 at five parallactic angles of the 500 MHz band (*left*) and the 32 MHz band (*right*). The red, green and blue data sets represent the Stokes Q (XX-YY), U (2XY) and V (2YX) signals normalized with respect to the Stokes I signals.

canning direction (along RA or Dec). Scanning speed is 15 arcsec s^{-1} by default. The schematic diagram of this mode is illustrated in Figure 21.

5. MultiBeamOTF mapping. This mode is proposed to map the sky with 19 beams simultaneously. Compared to the OTF mapping, the MultiBeamOTF mapping mode has a similar scanning trajectory but a larger separation (e.g., 20 arcmin) between parallel scans. Besides, the parameter of rotation angle is available in this mode.
6. MutiBeamCalibration. In this mode, 19 beams will be switched in sequence to track the calibrator, allowing for quick calibration of the gain of 19 beams in 30 minutes. Switching time between two beams is 40 s. The integration time for each beam is a parameter that

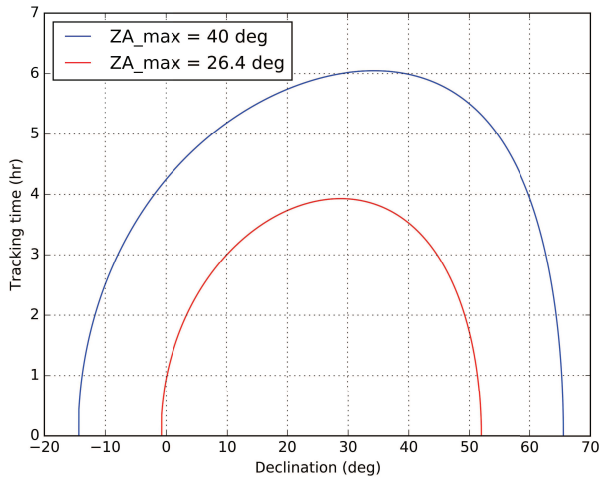

Fig. 20 Maximum tracking time for source at specific Dec. Results for ZA of 40° and 26.4° are represented with blue and red, respectively.

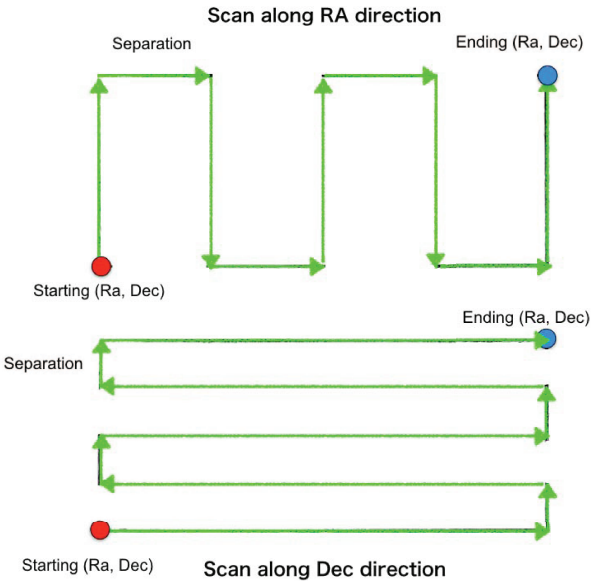

Fig. 21 Schematic diagram of OTF mode. The blue line represents scanning trajectory. The top and bottom panels show scan information along RA and Dec directions, respectively.

needs to be set. The schematic diagram of this mode is drawn in Figure 22.

7. BasketWeaving. This mode is to scan the sky along a meridian line. Scanning speed ranges from 5 to 30 arcsec s^{-1}. Setting parameters include starting time, starting Dec, ending Dec and duration time.
8. Snapshot. This mode is utilized to fully map the sky in a grid. This type of mapping is not a Nyquist sampling, but could map a region with relatively deep integration time. This is especially beneficial for pulsar searching. As shown in Figure 23, movement of the 19 beam receiver would ensure fully covering the sky along the same Galactic latitude. Necessary parameters include source name, beginning and ending coordinates (RA and Dec), observational time range and scanning speed (less than 30′ s^{-1}).

The above modes are currently available for observation at FAST.

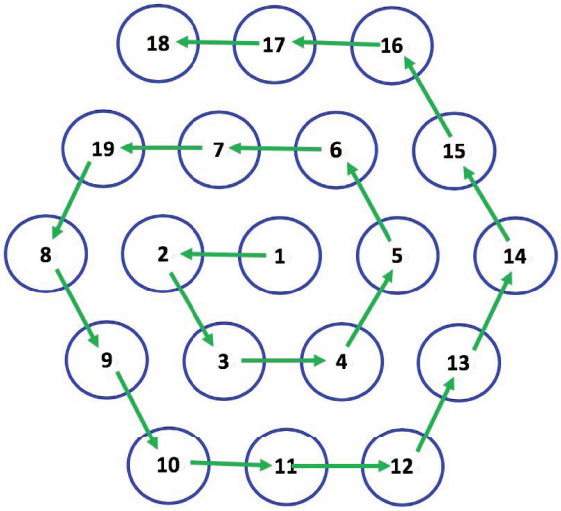

Fig. 22 Schematic diagram of MutiBeamCalibration mode. Green arrows represent the beam sequence for observing the calibrator.

4.2 Effect of Radio Frequency Interference

The current observation hints that RFI in FAST data is mainly divided into three types: narrow-band RFI, 1 MHz wide RFI and some wider fixed frequency RFI. Every type is discussed in more detail below.

1. The narrow-band RFI has always been ubiquitous through FAST data. We speculate that there are many origins, like interference from instruments or local influence of the telescope. For the FAST spectral data with a frequency resolution of 0.48 kHz (divided into one million channels in 500 MHz), they are extremely narrow and mostly only appear on one or several channels. Some of the narrow-band RFI could have high strength in a short integration time, but some of the others are just like a faint bulge without a Gaussian profile. In some cases, the narrow-band RFI tends to exhibit periodic variations in the time domain, which might be found in pulsar data if its time resolution is less than one second. The narrow-band RFI used to cause a lot of trouble for the FAST data processing, but it has now been resolved.

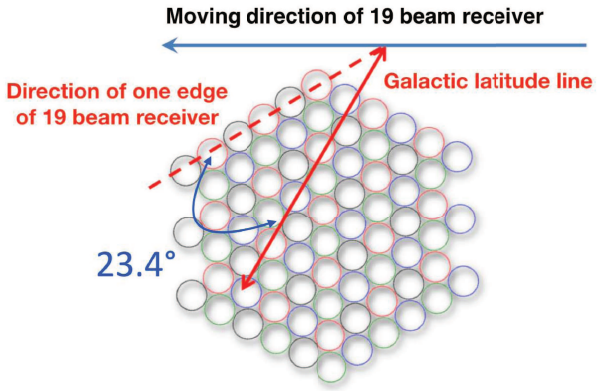

Fig. 23 Schematic diagram of snapshot mode. Blue line represents moving direction of 19 beam receiver. Dashed red line represents the direction of one edge of the 19 beam receiver. Galactic latitude line is represented with the solid red line. The angle between the dashed and solid red lines is 23.4°.

2. The 1 MHz wide RFI is caused by a standing wave, which looks like a regular sinusoidal wave or a single bump in FAST spectra. The big bump originates from the superposition of some standing waves with different amplitudes and periods. The typical width of this type of RFI is 1 or a few MHz. Existing *L*-band observations indicate that their distributions in time domain and frequency domain are not regular.
3. The fixed frequency RFI is due to satellite or civil aviation from the sky. It usually has a fixed frequency in a wider distribution, and has the strongest intensity in the whole bandpass, even improving the baseline there. Its spectral profile has a complex multi-peak structure, and the width of one peak might be around 20 MHz. The profile and intensity of it varies slightly in different observation times. In addition, the existence of such a sufficiently wide RFI may also be due to the higher sensitivity of FAST. It receives some very strong signal, which results in the frequency width of the response signal exceeding the range of satellite signal on both sides.

Since the successful installation of the EM shielding in April 2019, narrow-band RFI has been much reduced. Figure 24 demonstrates a comparison between the spectral results before and after installation of the EM shielding. They are observed on 2018 August 23 and 2019 April 20 in 10 minute integrations each day toward TMC-1, without periodic noise injection. These two days' results exhibit a significant decrease in RFI, suggesting the excellent result of the EM shielding. For some narrow line-width sources, such as Taurus, their molecular line width is within several or dozens of frequency channels and their RFI problems were previously very confusing. It is really satisfying that the tremendous reduction provides great convenience for the spectral line observation and identification. However, some 1 MHz wide RFI and fixed frequency RFI still exist in the present data..

In order to study the influence of human activities on FAST data and RFI signal, we observed for 10 minutes during daytime and nighttime in one day, supposing that human activity changes with day and night. The source of daytime observations was a quasar, observed at 15:00 on 2019 June 23. The night source was a star observed at 20:00 on the same day. Considering the beam dilution toward the point source and the extremely short integration time, we can assume that no signal from the day and night sources could be received except for HI emission from the interstellar medium. Therefore, ignoring HI, almost all of the emission in the obtained spectra should be RFI. Figure 25 shows the comparison of daytime RFI with nighttime RFI in *L* band. We can hardly see the narrow-band RFI emission in this figure, but the 1 MHz wide RFI is always present throughout the bandpass. The total amount of its signal is almost invariant, with no increase or reduction, but their central frequency slightly shifts from day to night. We magnified the axes of the Figure 25 to check for clearer movement, as displayed in the Figure 26. At the same time, the wider RFI from satellites and civil aviation is always located at the same frequency, just with a little variation in intensity.

Hoping to study the small frequency shift of the 1 MHz wide RFI as a result of the standing wave, we have drawn this exact movement in Figure 26. The center frequencies of RFI are marked as dash-dotted lines, which reveals that the systematic frequency shift of every RFI emission is all approximately 1 MHz in the figure, from daytime to nighttime. However, the 1 MHz shift does not apply to other FAST observations. We have checked the spectral data toward other sources. For the same source observed on different days, this type of RFI moves in different directions in the frequency domain, but within a few MHz. However, this shift is uncorrelated with source selection, and only changes in time. The current results imply that the direction to higher or lower frequency and the amplitude of such systematic shift in total bandpass is irregular. This behavior is in line with our speculation: This type of RFI which looks like a single bump is caused by the superposition of multiple standing waves, and such a superposition would make the spectra ever-changing. We have used this sinusoidal superposition to fit the baseline and the RFI could be removed well. In the future, we will try to do more to solve the problem of standing waves and RFI.

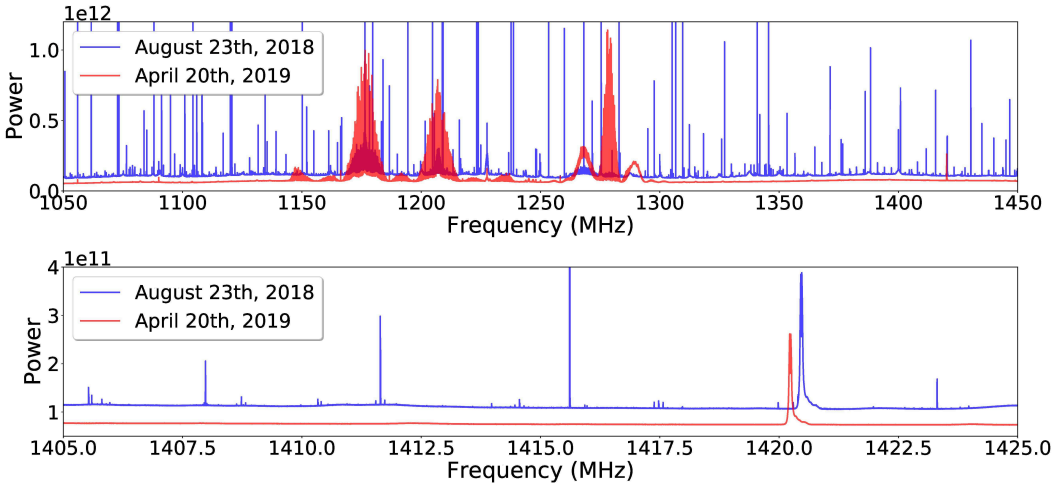

Fig. 24 Comparison of the spectral bandpass in 1000–1500 MHz (*upper panel*) and for HI spectrum at the frequency of 1420 MHz (*lower panel*) toward TMC-1 on different days, 2018 August 26 (*marked as blue line*) and 2019 April 20 (*marked as red line*).

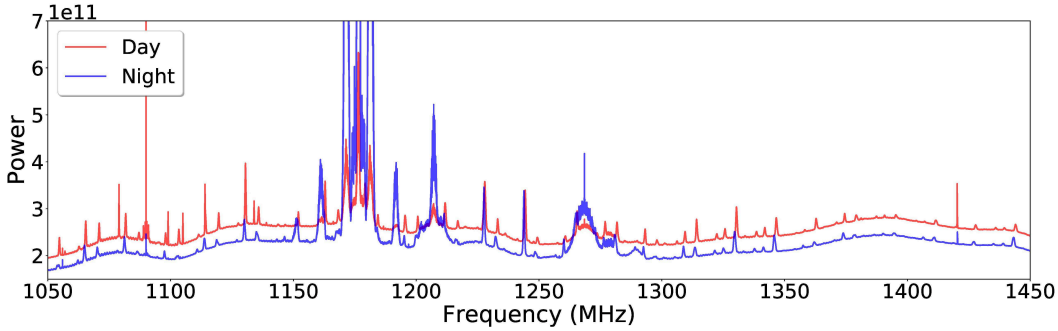

Fig. 25 Comparison of the bandpass in the daytime and nighttime with each 10 minute integration. The nighttime spectrum is marked as a blue line and the daytime one is marked as a red line.

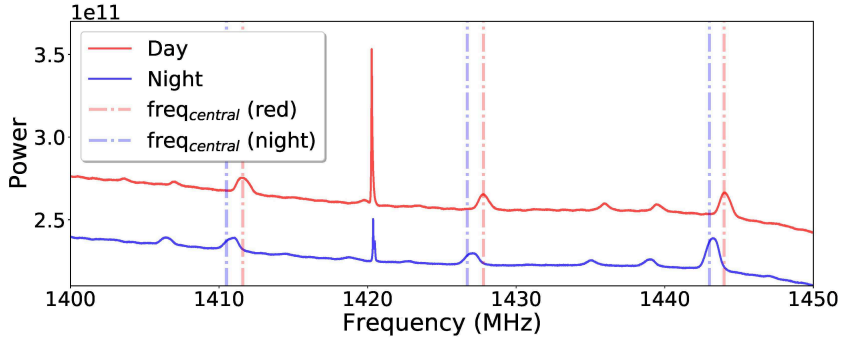

Fig. 26 Zooming in on the X and Y axes in Fig. 25, the systemic shift of this wide RFI is plotted. Red lines represent daytime and blue lines signify nighttime. The vertical dash-dotted lines indicate the center frequencies of a single RFI signal, making it easy to see the amplitude of the frequency shift from day to night.

5 SUMMARY

FAST has achieved its designed objectives. In this paper, we have presented the current status of FAST performances. They are summarized as follows.

1. The median power outputs of low and high noise diodes are around 1.1 and 12.5 K respectively. The measured temperature fluctuation of a noise diode is $\sim$ 1%, leading to $\sim$ 2% accuracy in flux calibration when pointing accuracy and beam size are included.
2. Spatial distribution and power pattern of 19 beams within ZA of 26.4° were obtained by mapping observations toward 3C 454.3. Beam width of 19 beams is consistent with theoretical estimation.

3. Pointing errors of the 19-beam receiver in different sky positions are less than $16''$. The standard deviation of pointing errors is $7.9''$.
4. The aperture efficiency as a function of ZA could be fitted with two linear lines at a specific frequency. It stays almost constant with ZA of 26.4° and decreases by $\sim 1/3$ at ZA of 40°.
5. The system temperature as a function of ZA could be fitted with a modified arctan function. This fitting is valid for ZA within 40°.
6. Fluctuation of the baseline is about 4% in 30 minutes. RMS of the baseline satisfies the expected sensitivity.
7. The standing wave has an amplitude of $\sim 0.3\%$ compared to continuum level. The amplitude and phase of the standing wave would vary at different ZAs during drifting. For position switch observations, standing wave of the residual ON-OFF spectrum would be suppressed with amplitude of ~ 0.02 K, which varies at different frequencies.
8. Derived polarization degree and polarization angle toward 3C 286 with FAST are $6.6 \pm 1.5\%$ and 33.4 ± 6.4 degrees, respectively. They are consistent with results from previous study.
9. Eight observation modes including drifting scan, total power, position switch, OTF, MultiBeamOTF, MultiBeamCalibrtation, BasketWeaving and snapshot are currently available for FAST observations.
10. RFI environment has been greatly improved in the last 18 months. Narrow RFI with several spectral channels is reduced. More effort will be done for eliminating broad RFI with width of ~ 1 MHz.

Acknowledgements We thank the beneficial discussion with Mao Yuan. This work is supported by the National Key R & D Program of China (No. 2017YFA0402701) and the National Natural Science Foundation of China (NSFC, Nos. 11673039, 11803051 and 11833009). TNY was supported by the CAS "Light of West China" program. LGH is additionally supported by the Youth Innovation Promotion Association CAS.

Appendix A: ELECTRONIC GAIN FLUCTUATIONS

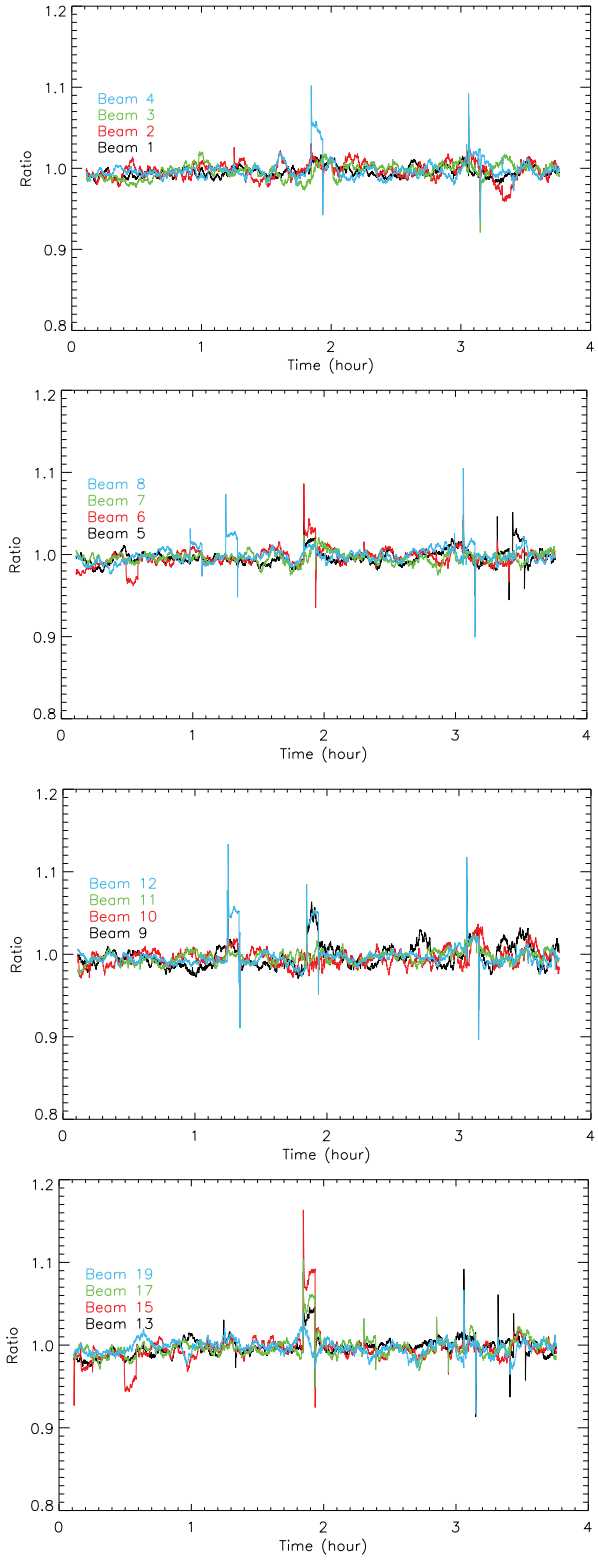

Fig. A.1 The electronic gain fluctuations of the system over several hours. The y-axis represents the ratio of fluctuations with respect to the mean temperature over time of Beams 1, 2, 3, 4, 5, 6, 7, 8, 9, 10, 11, 12, 13, 15, 17 and 19.

Appendix B: APERTURE EFFICIENCY

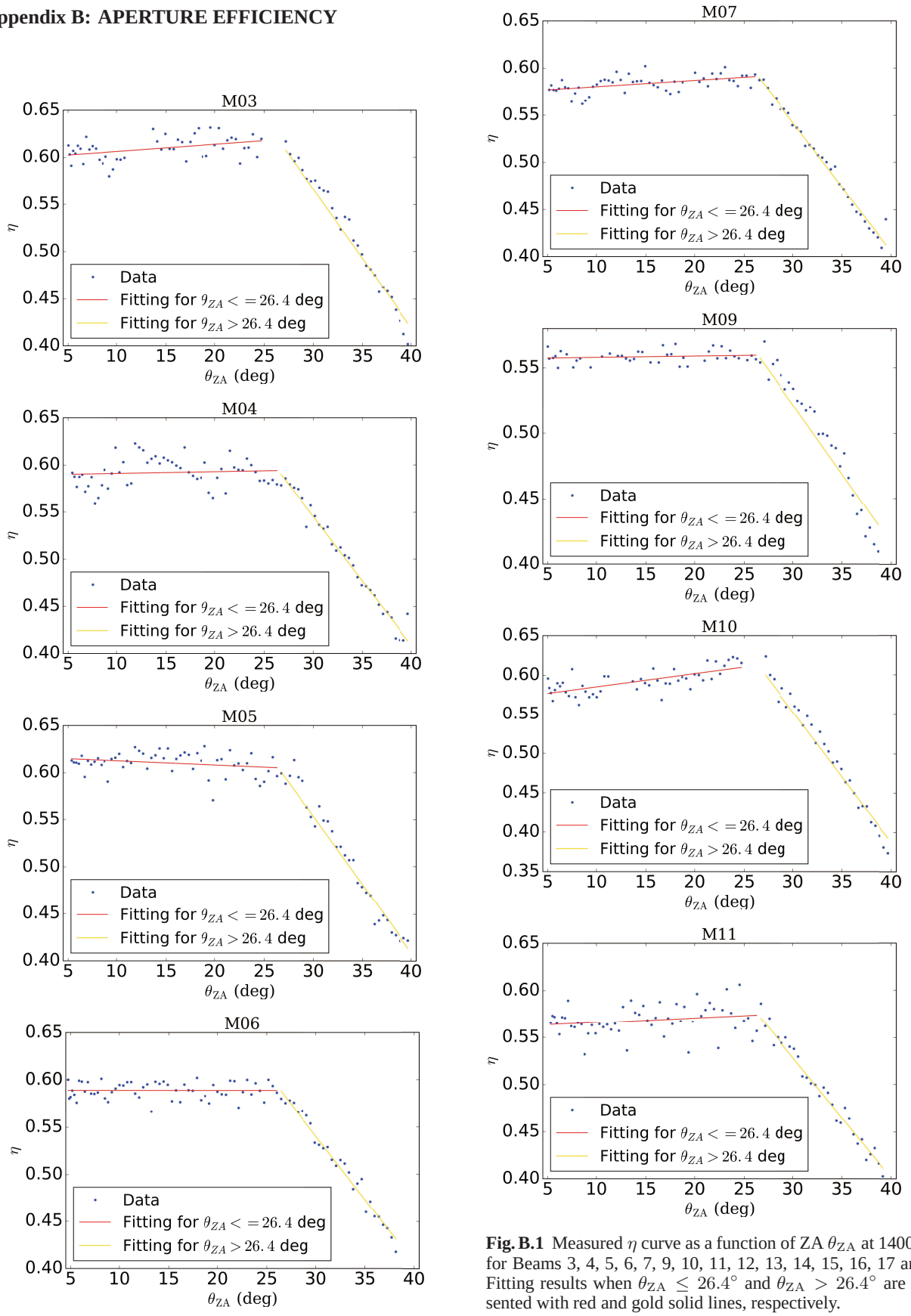

Fig. B.1 Measured η curve as a function of ZA $\theta_{\rm ZA}$ at 1400 MHz for Beams 3, 4, 5, 6, 7, 9, 10, 11, 12, 13, 14, 15, 16, 17 and 18. Fitting results when $\theta_{\rm ZA} \leq 26.4^\circ$ and $\theta_{\rm ZA} > 26.4^\circ$ are represented with red and gold solid lines, respectively.

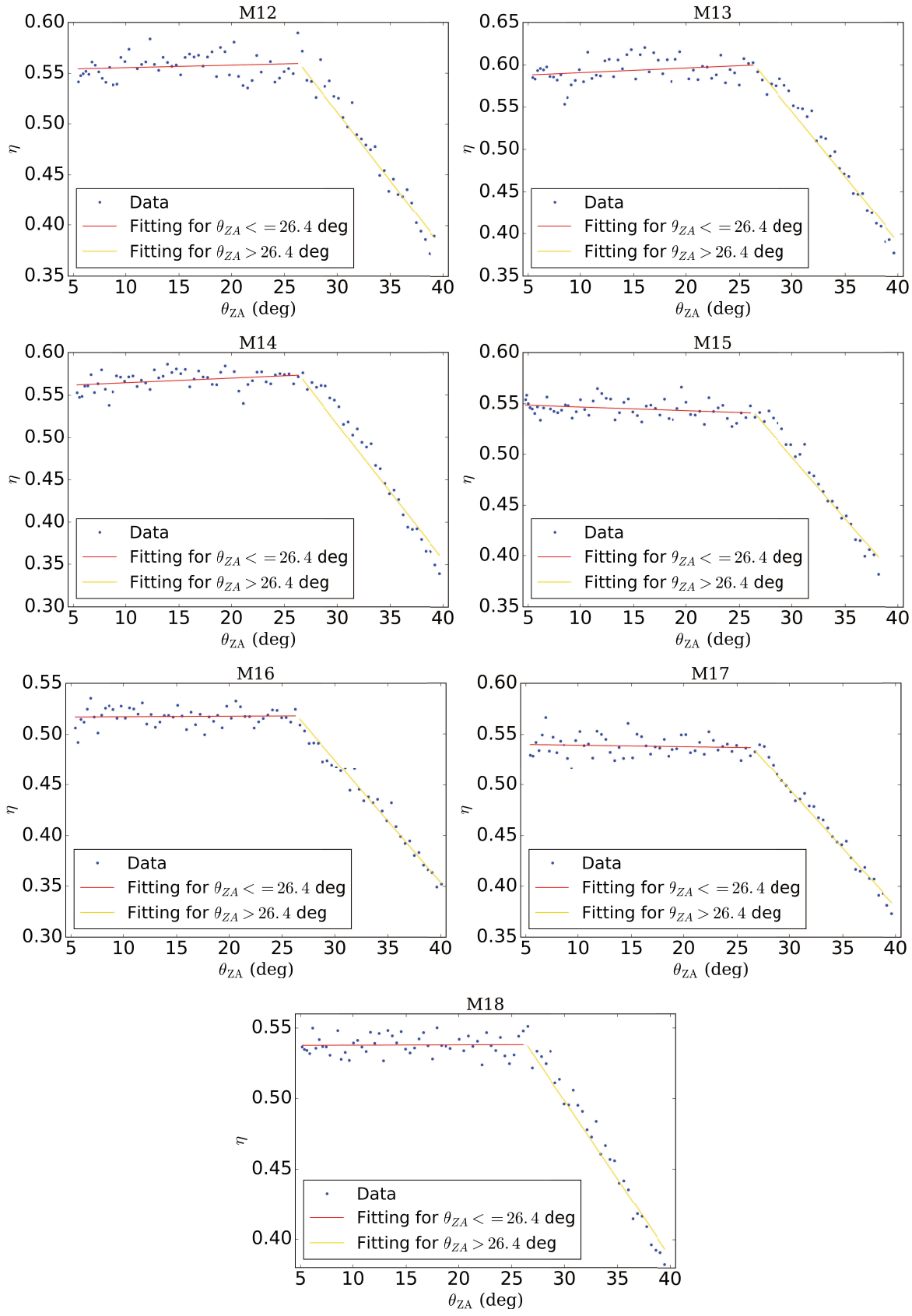

Fig. B.1 *Continued.*

Appendix C: SYSTEM TEMPERATURE

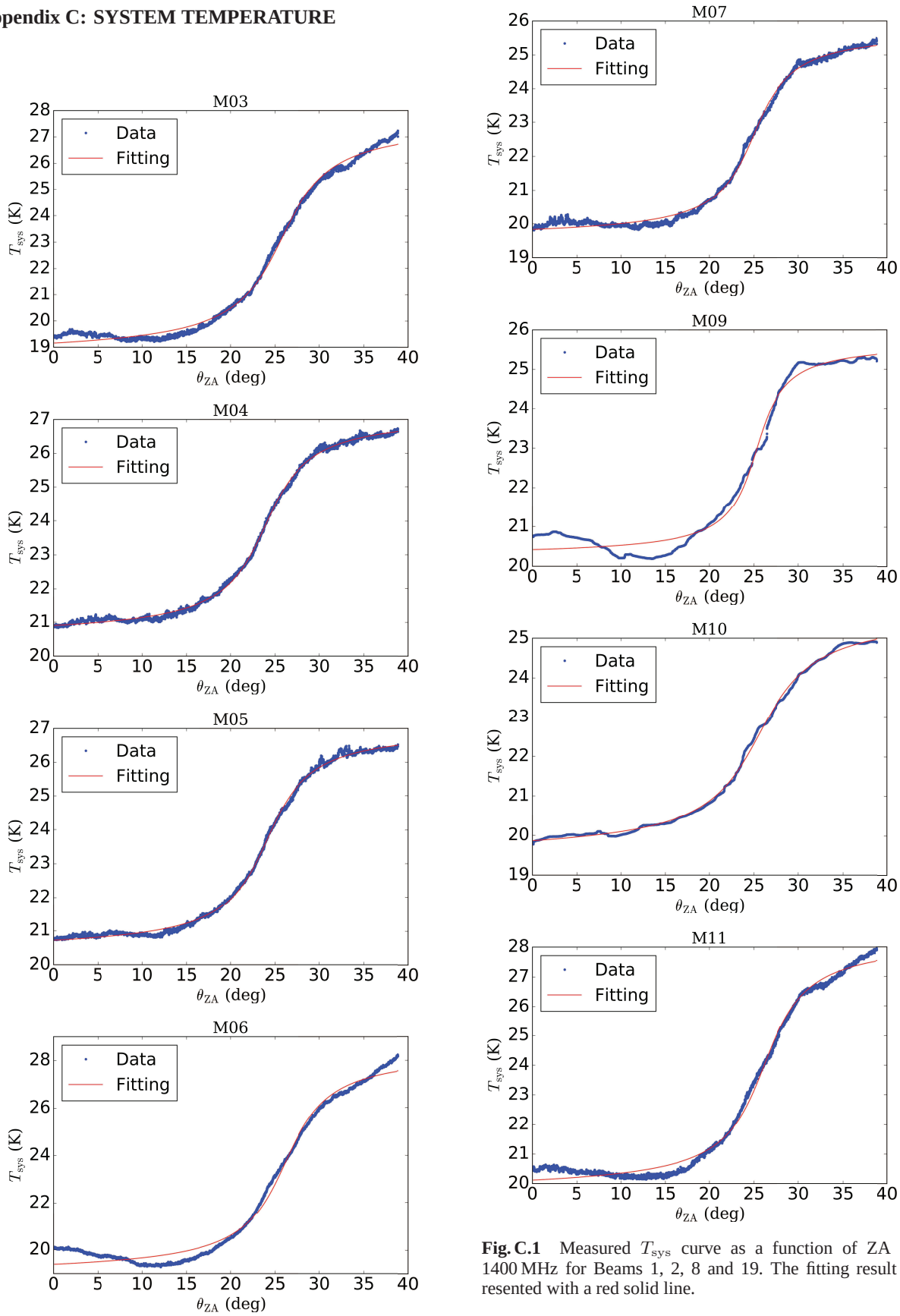

Fig. C.1 Measured $T_{\rm sys}$ curve as a function of ZA $\theta_{\rm ZA}$ at 1400 MHz for Beams 1, 2, 8 and 19. The fitting result is represented with a red solid line.

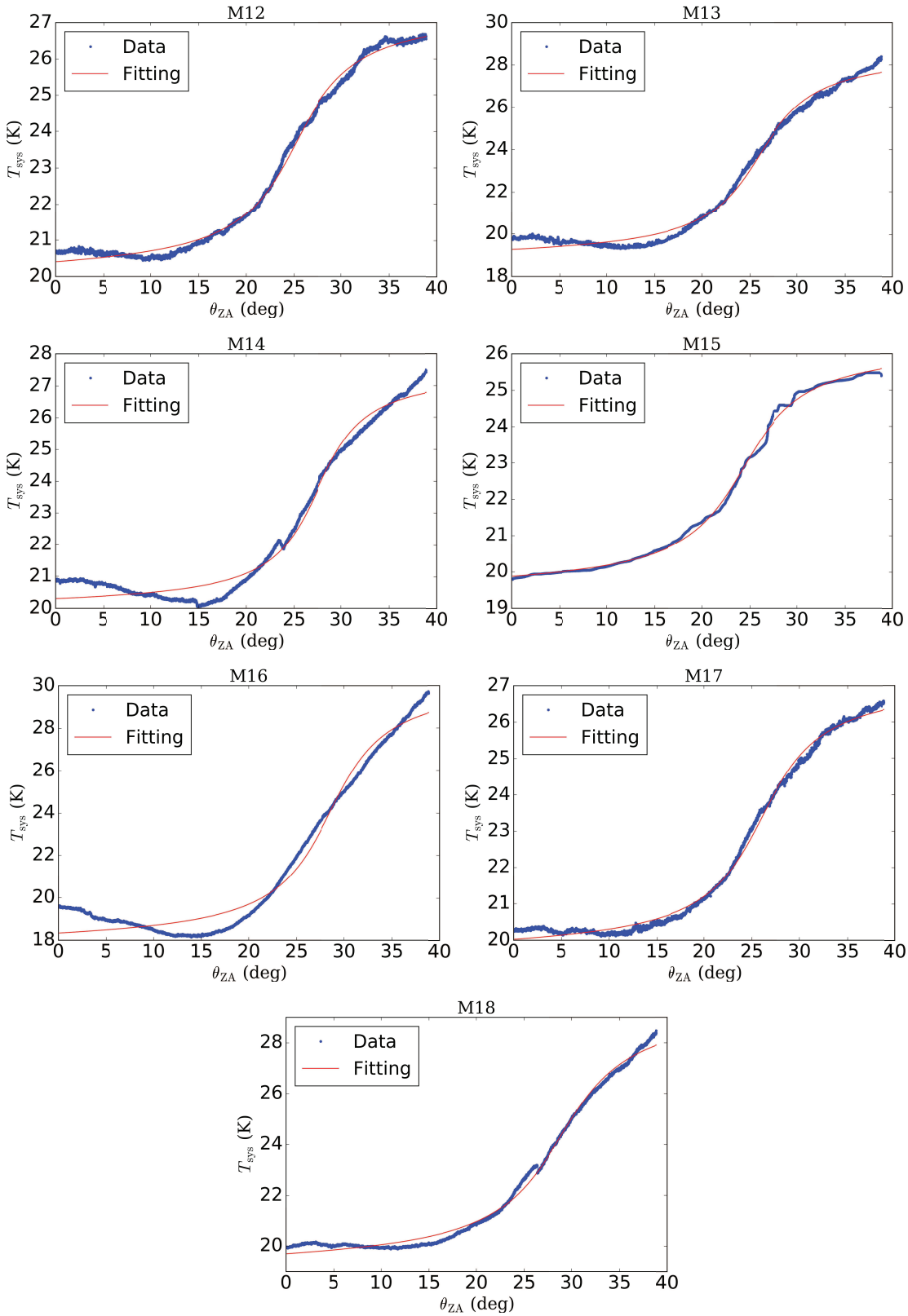

Fig. C.1 *Continued.*

References

Briggs, F. H., Sorar, E., Kraan-Korteweg, R. C., & van Driel, W. 1997, PASA, 14, 37

Calabretta, M. R., Staveley-Smith, L., & Barnes, D. G. 2014, PASA, 31, e007

Campbell, D. B. 2002, in Astronomical Society of the Pacific Conference Series, 278, Measurement in Radio Astronomy, eds. S. Stanimirovic, D. Altschuler, P. Goldsmith, & C. Salter, 81

Condon, J. J., & Yin, Q. F. 2001, PASP, 113, 362

Dunning, A., Bowen, M., Castillo, S., et al. 2017, in XXXIInd General Assembly and Scientific Symposium of the International Union of Radio Science (URSI GASS), Montreal, QC, 1

Heiles, C., Perillat, P., Nolan, M., et al. 2001, PASP, 113, 1247

Jiang, P., Yue, Y., Gan, H., et al. 2019, Science China Physics, Mechanics, and Astronomy, 62, 959502

Li, D., Wang, P., Qian, L., et al. 2018, IEEE Microwave Magazine, 19, 112

Lu, J., Peng, B., Liu, K., et al. 2019a, Science China Physics, Mechanics, and Astronomy, 62, 959503

Lu, J., Peng, B., Xu, R., et al. 2019b, Science China Physics, Mechanics, and Astronomy, 62, 959505

Perley, R. A., & Butler, B. J. 2013, ApJS, 206, 16

Perley, R. A., & Butler, B. J. 2017, ApJS, 230, 7

Popping, A., & Braun, R. 2008, A&A, 479, 903

Qian, L., Pan, Z., Li, D., et al. 2019, Science China Physics, Mechanics, and Astronomy, 62, 959508

Smith, S. L., Dunning, A., Bowen, M., & Hellicar, A. 2016, in 2016 IEEE International Symposium on Antennas and Propagation & USNC/URSI National Radio Science Meeting (APSURSI), Fajardo, 383

Wang, H., Zhu, W., Guo, P., et al. 2019, Science China Physics, Mechanics, and Astronomy, 62, 959507

Yu, Y.-Z., Peng, B., Liu, K., et al. 2019, Science China Physics, Mechanics, and Astronomy, 62, 959504

Zhang, K., Wu, J., Li, D., et al. 2019, Science China Physics, Mechanics, and Astronomy, 62, 959506